12-2019

Magnetic Properties of Nd-Fe-B Permanent Magnets Under Thermal Experimentation

Géraldine Houis
University of Nebraska-Lincoln, haldina@hotmail.fr

Houis, Géraldine, "Magnetic Properties of Nd-Fe-B Permanent Magnets Under Thermal Experimentation" (2019). *Mechanical (and Materials) Engineering -- Dissertations, Theses, and Student Research*. 149.
https://digitalcommons.unl.edu/mechengdiss/149

MAGNETIC PROPERTIES OF ND-FE-B PERMANENT MAGNETS UNDER THERMAL EXPERIMENTATION

By

Géraldine Houis

A THESIS

Presented to the Faculty of

The Graduate College at the University of Nebraska

In Partial Fulfillment of Requirements

For the Degree of Master of Science

Major: Mechanical Engineering and Applied Mechanics

Under the Supervision of Professor Jeffrey E. Shield

Lincoln, Nebraska

December, 2019

MAGNETIC PROPERTIES OF ND-FE-B PERMANENT MAGNETS UNDER THERMAL EXPERIMENTATION

Géraldine Houis, M.S

University of Nebraska, 2019

Advisor: Jeffrey E. Shield

Neodymium-Iron-Boron (Nd-Fe-B) magnets were developed in the 1980s, and since then, they have appeared as a common component in many fields. From the industry to consumers or defense applications, from turbines, computers, cellphones to most audio systems, Nd-Fe-B magnets are present everywhere. But when Nd-Fe-B magnets are applied to the motors of electric vehicles and wind-turbine generators, their temperature rises, therefore Nd-Fe-B-Dy magnets are used. However, while the use of these magnets is common at low temperatures, their properties decrease dramatically with the increase of temperature. In this paper, the Nd-Fe-B-based samples used were prepared by using arc melting, melt spinning, annealing (600-800°C, 10-20min), spark-plasma sintering (700°C, 30-40s), hot deformation, and grain boundary diffusion ($Nd_{70}Cu_{30}$, Pr-Cu-Al, $Nd_{62}Dy_{20}Al_{18}$). The objective of this paper is to get a better understanding of the magnetic properties (coercivity, remanence, energy product) of these magnets under different temperatures and with slightly different compositions and processes in order to find a correlation between them.

Acknowledgements

Many people have been involved in my thesis work and contributed not only with their knowledge and competence but also with their understanding and kindness.

First and foremost, I would like to thank Dr. Jeffrey Shield, my advisor, for offering me a chance to work on this interesting research project. He is always very kind and patient to answer my questions and giving me advices.

I would also like to take this opportunity to thank the members of my research group for their continuous support and help. Their cooperation was extremely kind and helpful.

Next, I would also like to thank my teachers from France for supporting and advising me all along.

Lastly, I would like to thank my friends and family who have stood by me throughout my academic career.

Reseach was supported by National Oilwell-Varco. The research was performed in part in the Nebraska Nanoscale Facility: National Nanotechnology Coordinated Infrastructure under award no. ECCS: 1542182, and with support from the Nebraska Research Initiative through the Nebraska Center for Materials and Nanoscience and the Nanoengineering Research Core Facility at the University of Nebraska-Lincoln.

Table of Contents

List of Tables

List of Figures

1. Introduction

1.1. Magnetism historical background

Magnetism goes way back, through almost 3000 years of history. Starting in Ancient Greece and China, the lodestone, a type of iron ore called magnetite (Fe_3O_4) used for compasses or “south-pointer”, is considered as the first use of magnets in history. Nevertheless, the Greeks were the ones who first started to write about the properties of magnetic iron FeO-Fe_2O_3 and the lodestone around 800 BC [1]. After a millennium of science and philosophy, Europeans knew that lodestone attracted iron, and that this attractive power was limited to a certain distance, but not that the strength of the attraction was decreasing with the distance itself. In the meantime, most likely in Egypt, the phenomenon of magnetic repulsion was discovered. [2] To summarize magnetism history, we can divide it into seven “ages” as shown in Table 1 [3], where the achievements are listed with the representative materials used in each period. In 1820, the Danish physicist H. C. Oersted demonstrated that a current-carrying wire produced a circumferential field capable of deflecting a compass needle, concluding that there is a relation between magnetism and electricity. In 1830, M. Faraday discovered that a changing magnetic field produces a current in a coil of wire and described the notion of magnetic field. The age of understanding marked a difference since it led to the commercialization of magnetic-based technologies around the world. [3] Magnetic research has been growing with time, especially during the 20th century, and new improvements keep coming, since fundamental understanding is not always necessary for that to happen. Indeed, the desire for discovery, understanding, optimization and improvement is expected to continue in the future.

Table 1: The seven ages of magnetism

Age	Time	Material	Achievements	Applications/Devices
Ancient	1000-1500	Iron, Lodestone	Force field, induced magnetism, thermo-remanence	South-pointer, compass
Early	1500-1820	Iron, Lodestone	Earth's field	Dip circle, Horseshoes magnet
Electromagnetic	1820-1900	Electrical steel	Electromagnetic induction, Maxwell's equations	Motors, generators, telegraph, wireless magnetic recording
Understanding	1900-1935	Al-Ni-Co Alloys	Spin, exchange interactions	
High frequency	1935-1960	Ferrites	Microwaves	Radar, television, magnetic resonance imaging
Applications	1960-1995	Nd-Fe-B, Sm-Co	New materials miniaturization of magnetic circuits	Consumer electronics
Spin electronics	1995-…	Multilayers	Thin films devices	High density magnetic recording

1.2. Fundamentals of magnetism

1.2.1. Units

There are two different systems of units used to express the magnetic properties listed in Table 2: the SI-Unit system (meter, kilogram, second) and the cgs-emu system (centimeter, gram, second, electromagnetic unit of magnetic moment). Concerning this thesis, the cgs-emu system is used for the results.

Table 2: Magnetic Units for SI and cgs-emu system

Quantity	**symbol**	**SI-unit**	**cgs-emu unit**
Magnetic field strength	H	Ampere/m [A/m]	Oersted [Oe]
Magnetic induction	B	Tesla [T]	Gauss [G]
Magnetic moment	m	Ampere m^2 [A.m^2]	emu
Magnetization	M	Weber/m^2 [Wb/m^2]	emu/cm^3
Permeability	µ	Henry/m [H/m]	Gauss/Oersted [G/Oe]

1.2.2. Magnetic moment

Electric currents and magnetized materials are two sources of magnetic fields, but the real origin of magnetism originates at the atomic level. There are many electrons in an atom, and they are revolving around the nucleus in their respective obits as well as spinning around their own axes. Note that an electron is punctual and thus cannot actually spin. The spin moment is intrinsic to the particle. This is further shown by the fact that the spin of an electron does not derive from impulse or position variables. If it did, it would be an integer like the orbital moment.

These movements create small magnetic fields with a magnetic moment shown respectively as vectors along the axis of the orbital motion and along the spin axis either up or down depending on the direction of its respective motion (right hand rule applies) [4] as shown in Figure 1. The interaction between these two moments is called spin-orbit coupling. The summation of the magnetic momentum of each individual orbital motion and spin motion gives us the net magnetic moment of an atom.

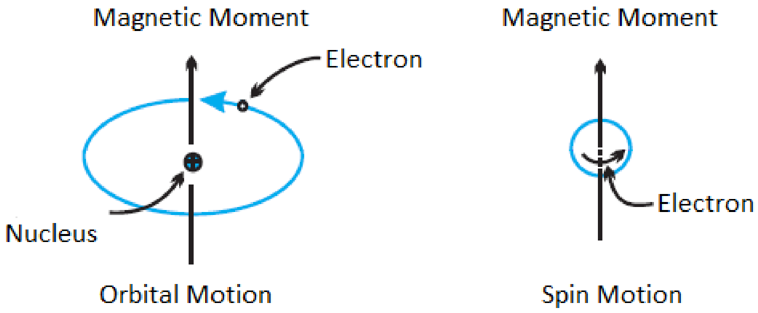

Figure 1: Magnetic moments due to orbital and spin motion

The magnetic moment is calculated by using the equation $m = \frac{-e}{2m_e}L$ where e is the unit of elementary charge, L is the angular momentum and m_e is the mass of an electron.

According to the Pauli exclusion principle, each atomic orbital may only be occupied by a maximum of two electrons, and the electrons in the same atomic orbital must have opposite spin which results in a cancellation of the spin and orbital moments, but most materials do not have full occupation of their orbitals. If a material is composed of atoms with a cancellation of spin and orbital moments, it will be unable to be permanently magnetized. Thus, the net magnetic moment of an atom has three contributions: the electronic spin, the angular moment, and the change in the orbital angular moment due to an external applied field. [5] If all the magnetic moments are random and their resultant magnetic moment is zero then this situation is called diamagnetism. On the contrary, if there is a resultant magnetic moment, it means that there is magnetization. The material can be paramagnetic, ferromagnetic, or antiferromagnetic, depending on the strength of the resultant moment and the orientation of spins. [5]

1.2.3. Types of magnetism

Diamagnetic materials are characterized by having a magnetic field response only when an external field is applied and being non-permanent magnets. Under an applied magnetic field, the magnetic moment is opposed to the applied field as shown in Figure 2. Common diamagnetic materials are copper, silver, carbon, lead, etc. [6]

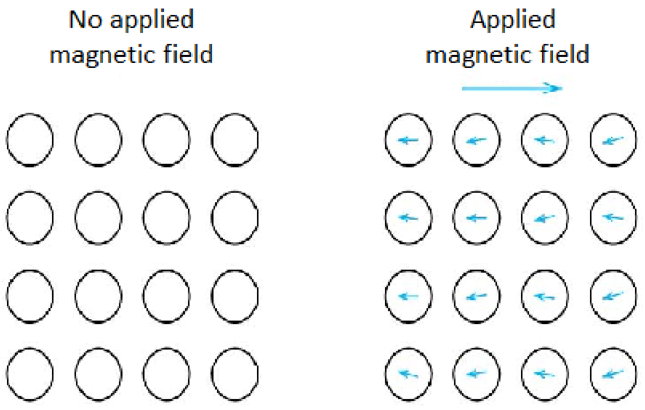

Figure 2: Atomic dipole configuration with and without an external applied field in the case of a diamagnetic material

Paramagnetic materials have atomic magnetic dipoles randomly oriented and have a zero-net magnetic moment, but under an applied field, they will have a magnetic moment in the same direction as the applied field as shown in Figure 3. Common paramagnetic materials are aluminum, magnesium, tungsten, etc. [6]

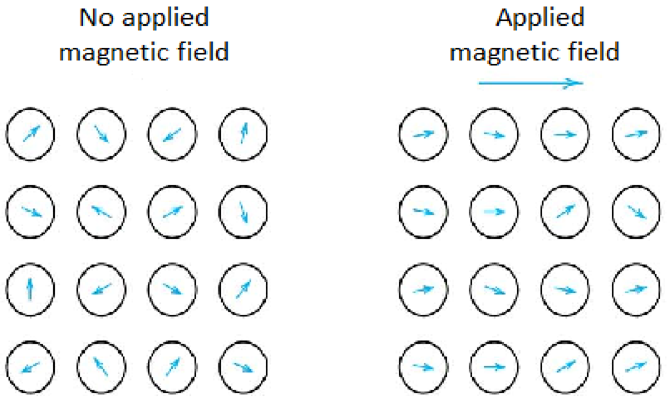

Figure 3: Atomic dipole configuration with and without an external applied field in the case of a paramagnetic material

Ferromagnetic materials have small regions where the magnetic dipoles are aligned resulting in a saturation magnetization inside each region called domain. There is a tendency for magnetic moments to orient themselves parallel to each other in addition to an external field. Common materials are cobalt, nickel, and some rare-earth materials.

Like ferromagnetic materials, ferrimagnetic materials can retain magnetization after the applied field is removed. But for ferrimagnets, the electrons tend to align themselves in opposite directions. However, the magnetic moments are different in magnitude so there is a net magnetic moment (Figure 4). Ferromagnetic and ferrimagnetic materials will become paramagnetic above the Curie temperature.

Antiferromagnetic materials have antiparallel dipoles which have the same magnitude resulting in a zero-net magnetic moment (Figure 4). Moreover, they react like paramagnetic materials under an applied field and become paramagnetic above the Neel temperature, but they cannot retain their magnetization when the applied field is removed. Common antiferromagnetic materials are chromium and manganese.

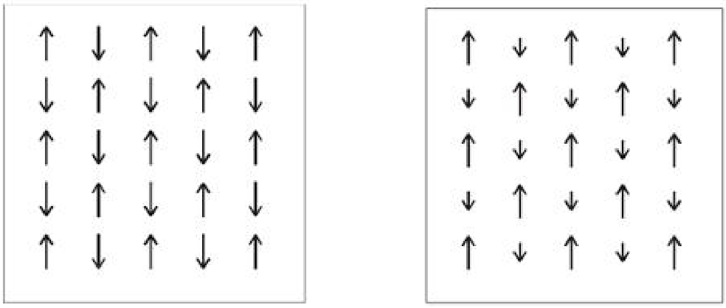

Figure 4: Representation of antiferromagnetic material (left) and ferrimagnetic material (right). The arrows represent the direction and magnitude of the atomic moments

1.2.4. Magnetic field, magnetic induction and magnetization

When a magnetic field H is applied to a material, the response of the material is called magnetic induction B. The equation relating B and H is as follows: [7]

$$B = H + 4\pi M$$

where M is the magnetization of the medium. The magnetization itself is defined to be the magnetic moment per unit of volume:

$$M = \frac{m}{V}$$

The ratio of M to H is called susceptibility (χ) and it indicates how responsive a material is to an applied magnetic field.

$$\chi = \frac{M}{H}$$

The ratio of B to H is called permeability (μ) and it indicates how permeable the material is to the magnetic field.

$$\mu = \frac{B}{H} = 1 + 4\pi\chi$$

1.3. Magnetic properties and characterization

1.3.1. Saturation magnetization

The saturation magnetization is the state in which the magnetization of the material no longer increases with the increase of the applied external magnetic field and the magnetization becomes stable. Moreover, the saturation magnetization is equal to the product of the net magnetic moment for each atom and the number of atoms present.

1.3.2. Hysteresis

Ferro- and ferrimagnetic materials retain their magnetization in the absence of a field. Moreover, reducing the field to zero does not reduce the magnetization of a magnet to zero which leads to a nonlinear response of its magnetization (M). This phenomenon is called a hysteresis loop. The B versus H graph is a typical hysteresis loop as shown in Figure 5. [8]

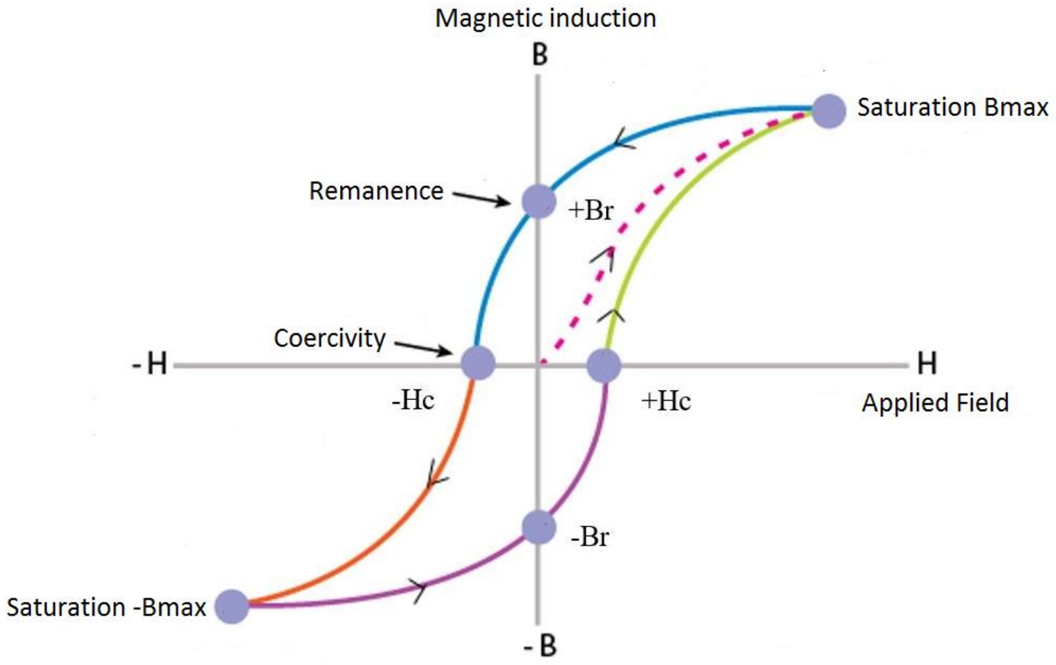

Figure 5: Typical B versus H hysteresis loop

The ferromagnetic magnets can have different types of hysteresis loops depending on their characteristics. Indeed, a low coercivity, high saturation magnetization, high remanence, and low energy product characterizes a soft magnet. Therefore, the hysteresis loop is narrow and thin. On the contrary, a hard magnet has a high coercivity, low saturation magnetization, low remanence, and high energy product. See Figure 6.

Therefore, the properties of a magnetic material could be optimized by forming a two-phase material with a soft and a hard magnet phase.

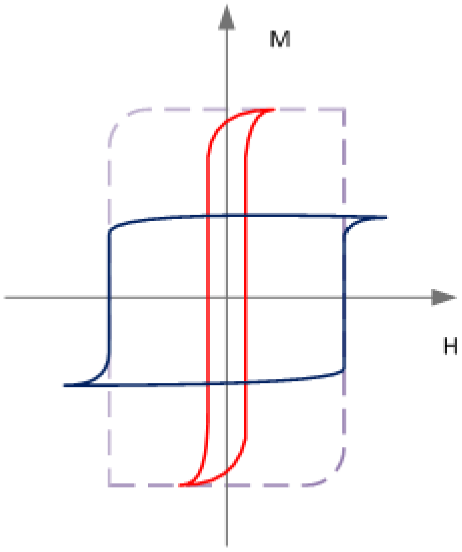

Figure 6: Characteristic hysteresis loops of a soft magnet (narrow and think) and a hard magnet (thick and large). The dashed loop would be the ideal magnet.

1.3.3. Coercivity

To reduce the magnetization to zero, an external magnetic field has to be applied in the opposite direction. The coercivity is the intensity of the reversed field that makes the magnetization equal to zero; therefore it represents the ability of a ferromagnetic material to withstand an external magnetic field without becoming demagnetized. See Figure 5. [9]

1.3.4. Remanence

The remanence is a measurement of the magnetic induction that remains in the magnet when the applied field is equal to zero. See Figure 5.

1.3.5. Energy product

The energy product [kJ/m^3] or [MGOe], is a measurement of the maximum amount of magnetic energy stored in a magnet. Its value is obtained with the maximum value of the product of the magnetic induction (B) and the applied magnetic field (H): (BH)$_{max}$. By using $B = H + 4\pi M$ with csg-emu units, we can determine the energy product. The (BH)$_{max}$ is the largest rectangle within the second quadrant of the B H curve shown in Figure 7. [8]

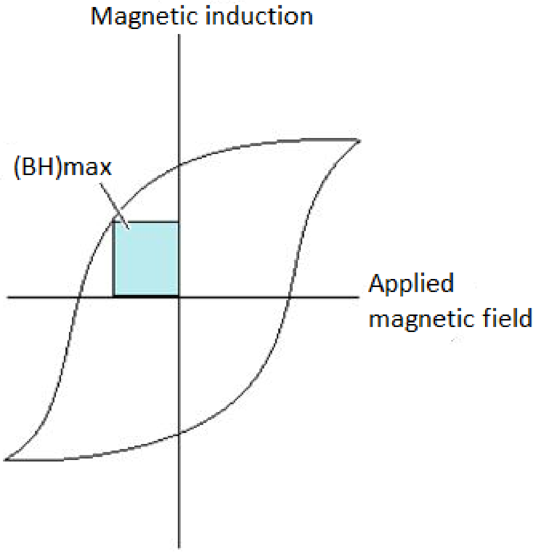

Figure 7: BH curve and energy product

Therefore, to obtain a better energy product, the coercivity and the remanence have to be optimized.

1.4. Types of anisotropy

The anisotropy is the origin of hysteresis and coercivity, and the anisotropy energy densities are very different for a soft magnet (0.0005 MJ/m^3) and a rare-earth permanent magnet (more than 10 MJ/m^3). [10] There are different types of anisotropy:

- Magnetocrystalline anisotropy is an intrinsic property and the most common source of anisotropy in a magnetic material. It involves electrostatic crystal-field interaction and relativistic spin-orbit coupling. Simply put, it is the necessary energy to deflect the magnetic moment in a single crystal from an easy to a hard direction. To minimize the magnetocrystalline anisotropy energy, the domains will form along the easy axes. See Figure 8. The area between the easy and hard axis curves gives the magnetocrystalline anisotropy energy for the concerned material.

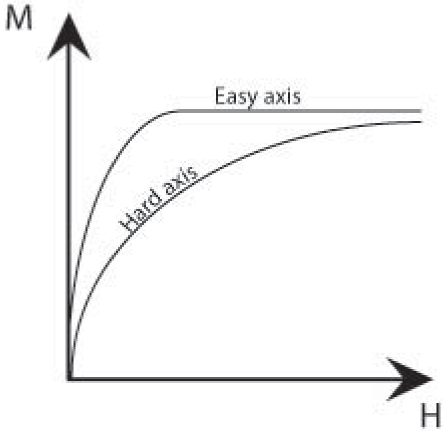

Figure 8: Field required to achieve the same magnetization along easy and hard axes

For a uniaxial anisotropy, the anisotropy energy can be expressed as follows:

$$\mathrm{E}_a = K \sin^2 \theta$$

where θ is the angle between the direction of M and the easy axis, and K is the anisotropic constant. [11]

Concerning rare-earth elements, they have a high magnetocrystalline anisotropy; therefore, once they have been magnetized, they will require a large opposite field to overcome the anisotropy and reverse the magnetization which is related to the coercivity itself. Yet, the anisotropy in all material decreases with the increase of temperature, and as it gets closer to the Curie temperature, there will be no preferred orientation for the magnetization. [10].

- Shape anisotropy: induced by the nonspherical shape of the grains.
- Stress anisotropy: the domain structure could be altered by an applied mechanical stress due to existing magnetostriction.
- Exchange anisotropy: occurs at the interface between an antiferromagnet and a ferromagnet when they interact.
- Anisotropy: induced by grain alignment and stress through magnetic annealing (thermostatic treatment).

1.5.Domains, domain walls, single domain particle

As previously discussed, a domain is a region where the magnetic dipole moments inside it are aligned in the same direction. The result is that there is a magnetization inside the domain in that direction. In the initial demagnetized state, the domains are arranged such that the magnetization averages to zero. Due to an external field, the domains, which are in the same direction as the external field, will start growing due to domain wall motion, while those opposing the field will start to reduce. If the applied field increases, the domain will overcome its anisotropic energy to orientate towards the direction and the applied field until all domains are aligned in the same direction. [12] See Figure 9.

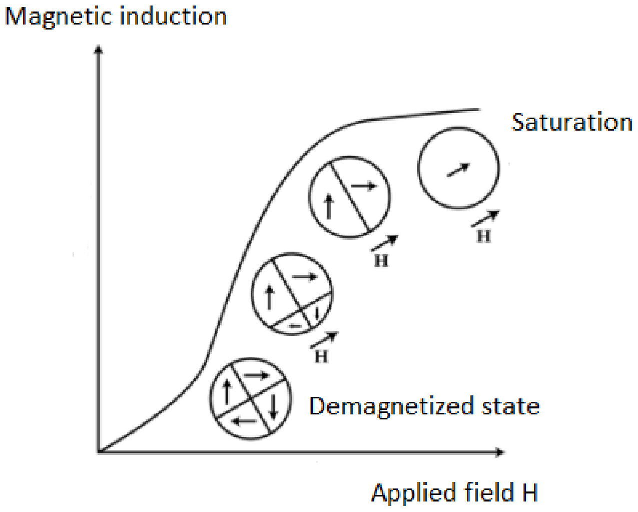

Figure 9: Domain orientation with magnetization

1.5.1. Domain energy

The total magnetic energy is, in relation with the exchange, the magnetostatic and the magnetocrystalline energies. The exchange energy is minimized when all magnetic moments are oriented in the same direction. However, the magnetostatic and the magnetocrystalline energies have larger contributions to the total energy. [12]

1.5.2. Domain walls

Domain walls are the regions between domains where the direction of magnetism must change, usually either 180° or 90°. The width of the domain is related to the exchange energy and the magnetocrystalline energy which form a balance.

$$\delta_0 = \sqrt{\frac{A}{K_1}}$$

where A is the exchange stiffness coefficient and K_1 is the leading term in magnetocrystalline anisotropy.

The most favorable domain walls are those which do not require an external demagnetizing field: the twist boundary (block boundary conditions) where the magnetization perpendicular to the boundary does not vary across the domain wall so no demagnetizing fields are generated, or the tilt boundary (Néel) where the magnetic moments rotate such that a constant angle is maintained between them and both the wall normal and the surface. The Néel wall occurs in thin films whose magnetic moments rotate around an axis perpendicular to the surface of the film. [12]

1.5.3. Single domain

Under a certain particle radius, it is energetically unfavorable to form domain walls, and instead a single-domain particle is formed [13]. The magnetic behavior of the material in a single domain system is affected by the domain wall motion. Indeed, there is a size dependence on the coercivity: single domain particles exist below a critical diameter where we can obtain the maximum value of coercivity. Smaller grain sizes are controlled by an interaction through grain surfaces because the surface properties are predominant at this scale. Coercivity will approach zero when the particle diameter is decreasing until it reaches a critical diameter D_p after which the coercivity remains constant at zero. Therefore, D_s is the ideal particle size with a single domain and maximum coercivity. See Figure 10.

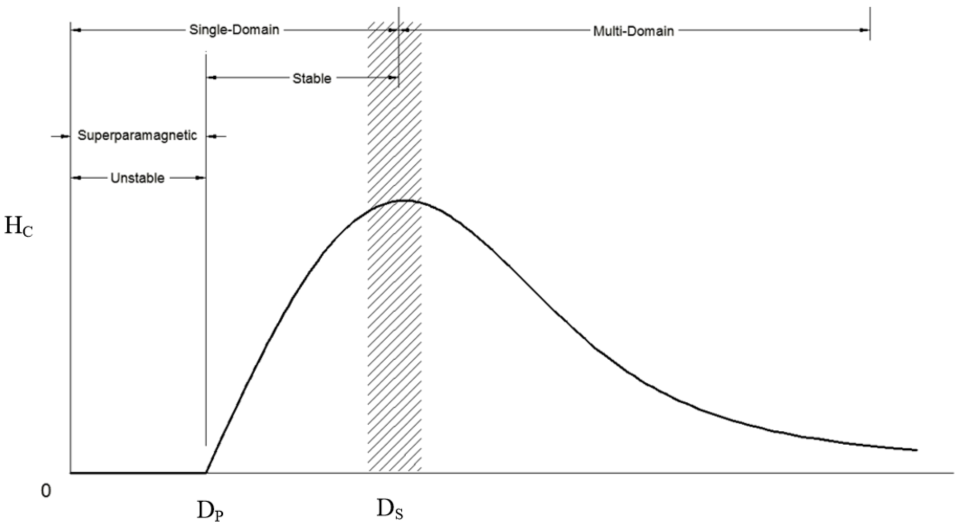

Figure 10: The effects of decreasing the particle size on coercivity with D_s as the ideal particle size with a single domain and maximum coercivity [13]

1.6. Objective of the study

The objective of the study is to focus on Nd-Fe-B magnets´ magnetic properties from room temperature up to 200°C. Some of the samples had to be produced to establish reference results due to oxidation of the original available samples (melt-spun ribbons). The produced samples were $Nd_8Fe_{87}Nb_{0.5}Zr_{0.5}B_4$ and $Nd_{13.6}Fe_{73.6}Co_{6.6}B_{5.6}Ga_{0.6}$. The remaining samples were from other studies in order to avoid wasting rare-earth material and raw metals. To obtain the maximum information, samples with different processes such as annealing, spark plasma sintering, hot deformation, grain boundary diffusion, and the addition of Dy, Co, Ga, Nb, Zr, Dy-Co, Pr-Cu-Al were studied under different temperatures (room temperature, 50°C, 100°C, 150°C, 200°C) to find a correlation between the effect of temperature on magnetic properties and the composition of the sample, as well as its processing.

2. Literature review

2.1. Rare-earth permanent magnet materials

Rare-earth permanent magnetic materials are based on rare-earth elements such as Sm, Nd, Pr, and transition metal elements such as Co or Fe which have strong exchange coupling, high Curie temperature and high saturation magnetization, and very high coercivity and anisotropy field. The combination of elements helps to create an optimized magnetic material with higher energy product, coercivity, remanence and stability. High energy magnetic materials are also often used in place of electromagnets because they continuously maintain magnetic fields and generate no heat during operation.

2.1.1. History of permanent magnets materials

As previously discussed, permanent magnets have the unique ability to retain their magnetism after the removal of an applied magnetic field. This is due to their high magnetocrystalline anisotropy and the stability of their magnetization direction with respect to their crystal axes.

Through the first half of the 1900s, most permanent magnets were Fe-based alloys. The first improvement of $(BH)_{max}$ was achieved with the alnicos, discovered in 1931 by Mishima. [14] In the 1960's, permanent magnets based on intermetallic compounds and oxides appeared. The breakthrough came when Sm-Co-based compounds were introduced [15]. At first, K. J. Strnat et al. [16] developed a $SmCo_5$ phase in 1967 with a $(BH)_{max}$ of 5.1 MGOe. Then, in 1969, Das et al. [16] managed to increase it to 20 MGOe by applying the powder metallurgy process to the preparation. Later, permanent magnets based on Sm_2Co_{17} were developed with a $(BH)_{max}$ of 32 MGOe. [17] Nd-Fe-B magnets appeared simultaneously in the US and in Japan in the 1980s with a $(BH)_{max}$ of 37 MGOe. However, through processing and alloy optimization, this value has now increased up to 55 MGOe. [18]

2.1.2. Nanocomposite permanent magnets

Nanocomposite magnets or nanocrystalline exchange coupled permanent magnetic materials consist of a mixture of magnetically hard and soft phases as mentioned earlier. The hard phase brings high coercivity, low remanence, and high energy product, while the soft phase brings high magnetization, high remanence and low coercivity. Mixing these two phases is called exchange coupling which alloys the spins of the soft phase to interact across grain boundaries and to lock into alignment with the hard phase. [19] The only condition is that the soft phase must be of nanoscale dimensions, approximately twice the width of the domain wall in the hard phase, so that its magnetic moments are exchange coupled with the hard phase. [15] This is related to the fact that these exchanges occur between single domain particles. Indeed, single domains have a critical maximum radius; above this radius, it is more energetically favorable to form multiple domains. [12]

The critical dimension of the soft phase is calculated by $\delta_h = 2\pi\sqrt{A_h/K_h}$ where A_h and K_h are, respectively, the exchange and anisotropy constants of the hard magnetic phase.

2.1.3. Neodymium-Iron-Boron Magnets

Currently, the most common two-phase nanocomposite rare-earth permanent magnetic materials are $Sm_2Fe_{17}Ny$ and $Nd_2Fe_{14}B$, and the soft magnetic phase is mainly α-Fe or Fe_3B. The $Nd_2Fe_{14}B$ is currently the strongest permanent magnet with a theoretical energy product of 64 MGOe for anisotropic materials, but there is always motivation to develop materials with a higher energy product especially for elevated temperature applications. In the $Nd_2Fe_{14}B$ compound with an α-Fe soft phase, the Fe provides most of the magnetization and yields a higher Curie temperature. The Nd is at the origin of the magnetocrystalline anisotropy and the B is used to stabilize the tetragonal structure of $Nd_2Fe_{14}B$, which has a space group of $P4_2/mnm$. It has been reported that $Nd_2Fe_{14}B$ usually exhibits a structure which is layered with stacking sequence of one Nd-rich layer and Fe sheet. [20]

This nanocomposite is usually prepared by rapid solidification techniques such as melt-spinning. We can observe the phase diagram of the system as shown in Figure 11.

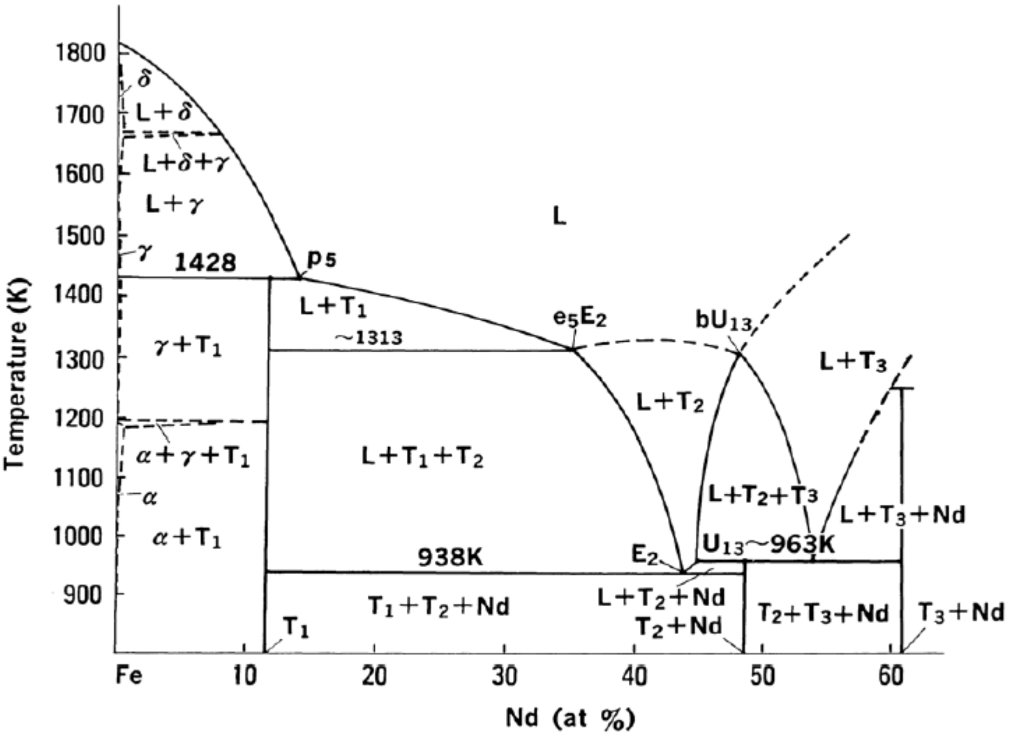

Figure 11: The pseudo binary diagram of the Nd-Fe-B ternary system [21]

It is understood that the cooling rate affects the microstructure. Therefore controlling the speed of the wheel makes it easier to obtain the 2-4-1 phase and the amount of α-Fe.

2.2. Addition of elements to Nd-Fe-B magnets

In order to improve the corrosion resistance, most efforts have been focused on the addition of alloying elements such as Co, Ga, and Cu.

Pandian et al. [22] tried the Co addition but it resulted in a decrease of coercivity even for a small addition. This was attributed to the formation of new phases, such as $Nd(Fe,Co)_2$ and $Nd(FeCo)_3$, with ferromagnetic behavior. However, they obtained an improvement of the Curie temperature of the magnet and a higher energy product when compared to the sample without the Co addition.

The addition of Dy can increase the anisotropy field, refine the grains, and increase the coercivity, but it decreases the remanence, saturation polarization, and energy product of the magnet. The optimal content for global good magnetic properties is 3-4%wt [23]. This is due to the effects of the Dy addition on the anisotropy field of the hard phase and the microstructure of the magnets. Additive Dy atoms enter the hard $Nd_2Fe_{14}B$ phase, substitute into Nd sites, and form $Dy_2Fe_{14}B$, which has a larger anisotropy field than that of $Nd_2Fe_{14}B$ and thus increases the coercivity. Moreover, a Dy addition can suppress the separation of α-Fe branch crystals when the melted alloy solidifies, making the grain of the magnet uniform and fine [24].

Indeed, to obtain a good coercivity at an elevated temperature, a room temperature coercivity of around 30KOe (3T) is needed in Nd-Fe-B magnets. To meet this requirement, a relatively large amount of Dy is used, and since the magnetic moment of Dy is coupled antiparallel to that of $(Nd_{1-x}Dy_x)_2Fe_{14}B$, it leads to a decrease of the energy product. [25]. A magnet with 30% of the Nd component replaced with Dy presents a superior high temperature performance. [26]

The addition of the right amount of Ga increases uniaxial anisotropy by forming the Nd-rich intergranular phase containing Ga. This new intergranular phase lubricates the grain boundaries and weakens the exchange-coupled demagnetization effect by improving the soakage property of the liquid phases. Non-magnetic Ga atoms enter the hard $Nd_2Fe_{14}B$ phase to substitute on Fe sites, which leads to increased uniaxial anisotropy and subsequently enhances the coercivity of the magnet. [23]

With the addition of Dy, Ga and Co in the right proportions, G. Bai et al. [23] obtained a -0.53%/°C temperature coefficient of coercivity (20-150°C) of the magnet which satisfies the needs of permanent magnet motors. The $(BH)_{max}$ was 39.9 MGOe, and the coercivity 25.57kOe at room temperature. Pandian et al. [22] also concluded that the combined addition of Dy, Ga, and Co to Nd-Fe-B showed an increased Curie temperature, a considerable improvement of coercivity and the reduction of the remanence was <5%.

R.S. Mottram et al. [27] studied the addition of Nb and concluded that, with the correct amount, it showed moderate improvements in coercivity and temperature stability. It is usually found distributed throughout the microstructure either as small precipitates or as grain boundary phase. The precipitates are thought to improve coercivity by pinning grain growth during sintering. [27]

2.3. Spark plasma sintering (SPS)

2.3.1. Principle of the SPS process

Spark plasma sintering (SPS), also known as field assisted sintering (FAS), pulsed electric current sintering (PECS), plasma assisted sintering (PAS), or plasma pressure consolidation (PPC), is a newly developed rapid sintering technique to achieve fast densification results with minimal grain growth in a short sintering time. [28]

The SPS process reduces the grain growth during consolidation because of the application of a short sintering time, rapid heating, and low-temperature sintering.

The SPS process is based on the theory of high-temperature plasma momentarily being generated in the gaps between powder materials by electrical discharge during DC pulsing. Application of rapid heating results in bypassing low-temperature regions where surface-transport controlled sintering is dominant.

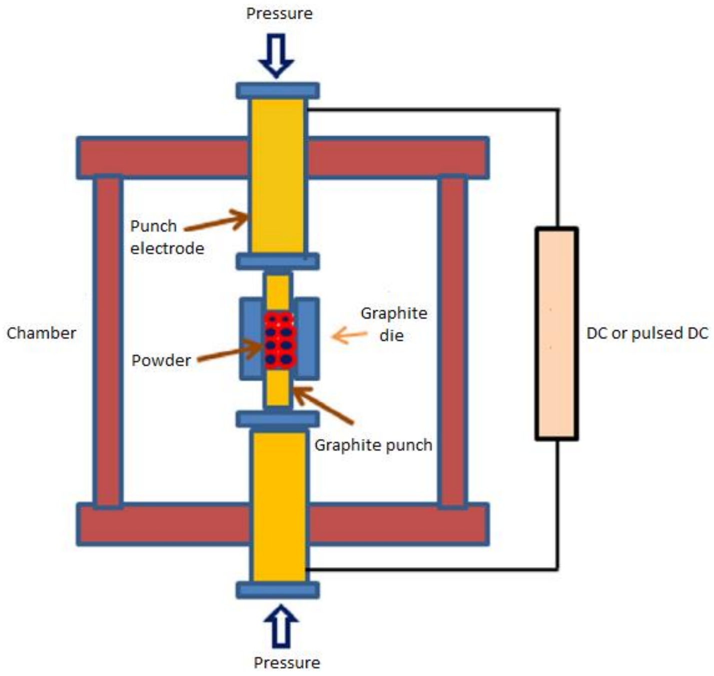

Figure 12: Schematic representation of spark plasma sintering technique

The schematic representation of SPS is displayed in Figure 12: SPS provides pressure through a vertical single-axis direction and the punch electrodes have an internal water cooling system. The sintering chamber is also water-cooled. The atmosphere within the chamber is either a low atmospheric pressure or a protective gas environment. The powder samples are stacked within the graphite die and between two punches.

However, the nature of the activation effects is not clearly established. The most basic proposed idea suggests the ON-OFF DC pulse energizing method generates spark plasma, spark impact pressure, Joule heating and an electrical field diffusion effect. The key characteristics of SPS can be summarized as follows: the generation of a local electric plasma discharge and its effect on heat and mass transport in a particle body, the combined effect of external fields (force and electric) on the densification and phase formation in a particulate system, the influence of electric current in the near surface layers of conductors and semi-conductors (skin-effect) as well as dielectrics at elevated temperatures, and the rapid non uniform heating/cooling throughout the sample (large temperature gradient). [29] The typical current path is illustrated in Figure 13.

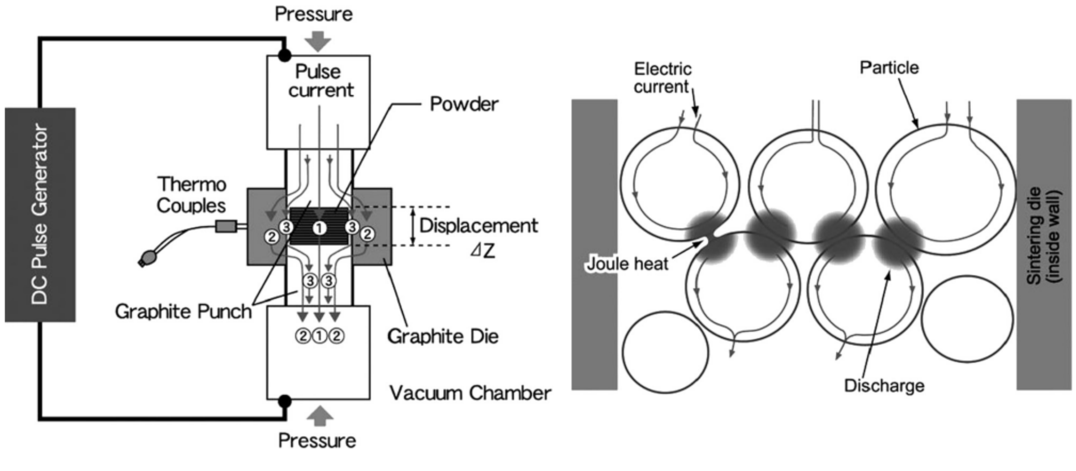

Figure 13: ON-OFF DC pulsed current path and pulsed current flow through powder particles [30]

2.3.2. Sintering of Nd-Fe-B permanent magnets by SPS

Since the SPS technique was found suitable for the preparation of nanocrystalline Nd-Fe-B magnets in 1984, it has been playing an important role in the production of fully dense rare-earth permanent magnets [31].

During the sintering process, an anisotropic alignment of the $Nd_2Fe_{14}B$ phase occurs, leading to a higher energy product. Therefore, SPS-processed Nd-Fe-B magnets are critical components for numerous devices ranging from electric motors to disk drives, as well as traction motors and wind generators [25].

Yue et al. [32] also determined that SPS-processed magnets have a better corrosion resistance and better mechanical properties than most magnets produced with conventional densification process.

Liu et al. [33] studied the SPS process and its influence on the microstructure. They noticed two distinguishable zones with different grain sizes that affected the magnetic properties, the coarse grain zone (grain boundary area) and the fine grain zone (interior of particle). From that, they determined that above a certain sintering temperature, the grain growth was excessive and degraded the magnetic properties of the sample at room temperature, and even more at elevated temperatures.

Sugimoto [25] studied the improvement of thermal stability for Nd-Fe-B magnets and determined that it is directly linked to the increase of coercivity. The Nd-rich phase becomes a liquid phase at temperatures above 665 °C and enhances densification during the sintering process. The liquid phase is present along grain boundaries cleaning the surface of $Nd_2Fe_{14}B$ grains and decreasing the number of nucleation sites. Therefore, Nd-Fe-B sintered magnets use the Nd-rich composition.

However, the Nd-rich phase is a non-magnetic phase and is easy to oxidize. The oxidation causes the precipitation of the soft magnetic phase, such as α-Fe at the surface of the main phases, which results in a decrease in coercivity. Therefore, the volume fraction of the Nd-rich phase should be as low as possible and the composition of the sintered magnets should be close to the stoichiometric composition of $Nd_2Fe_{14}B$ [25].

The SPS process can be improved by using a rare-earth grain boundary phase. It has a lower melting temperature and becomes liquid before the temperature reaches the sintering temperature. Different rare-earth rich phases can be used, but in every case they modify the microstructure of the magnet to enhance its magnetic properties. The ribbons obtained after melt-spinning are crushed into powders and mixed with low melting temperature alloy powders.

- Nd-Cu

The purpose of mixing Nd-Cu is to maintain the coercivity. Since the melting temperature of Nd-Cu is lower than the sintering temperature, it becomes liquid and diffuses along the grain boundaries of $Nd_2Fe_{14}B$ grains during the sintering process. During the sintering, the liquid phase along the grain boundaries helps to maintain the uniform microstructure, which is important for a high coercivity. In addition, this Nd-rich phase in the grain boundaries isolates the $Nd_2Fe_{14}B$ grains to some extent, also helping to maintain a high coercivity. [34]

- Dy-Cu

Lee et al. [35] tried to mix Nd-Fe-B magnet with different low-melting eutectic alloys such as Nd-Cu and Dy-Cu. The purpose of mixing Dy-Cu, was to improve the coercivity of the SPS-processed sample. Moreover, the Dy-Cu alloy has a higher melting point than the Nd-Cu alloy and the mixed samples obtained a higher coercivity. [35]

Dy-Cu has the same function as Nd-Cu. However, the diffusion of Dy-Cu along the grain boundaries increases the magnetic anisotropy of the sample by the partial substitution of Nd with Dy in the $Nd_2Fe_{14}B$ grain surface to form a $(Nd_{1-x}Dy_x)_2Fe_{14}B$ shell which has a higher magnetic anisotropy field than $Nd_2Fe_{14}B$. This high anisotropy suppresses the nucleation of the reverse domain, leading to a higher coercivity [36].

- Pr-Cu-Al

As previously discussed, the non-uniformity of the structure (fine and coarse grained zones), results from excessive temperature differences between the surface and the center of the starting powders as the Joule heating is concentrated along particle boundaries. The method proposed by Zhang et al. [37] is to add a low-melting-point alloy that aids the consolidation of the Nd-Fe-B powder particles and absorbs the brunt of the excessive temperatures. The addition of a low-melting-point alloy such as $Pr_{68}Cu_{25}Al_7$ (melting point 432°C) can effectively suppress the formation of coarse grain zones and enhance the coercivity of SPS magnets. [37]

2.4. Hot deformation (HD)

Lee et al. [38] originally developed the hot-deformation process of rapidly solidified Nd-Fe-B ribbons and managed to produce anisotropic magnets with an ultrafine grain size of nearly a single domain size. The coercivity of conventional sintered Nd-Fe-B magnets deteriorates when the grain size becomes smaller than 3µm because of the oxidation of fine rare-earth alloy powders.

Hioki et al. [39] reported that both coercivity and the temperature coefficient of coercivity can be improved by decreasing the average grain size. They observed that the domain wall pinning is dominant in the magnetization reversal in the Nd-Fe-B hot-deformed magnet. Finally, they concluded that, for hot-deformed magnets, coercivity and its temperature dependence significantly improve if a sharp grain boundary interface can be realized.

The HD process is commonly used to achieve good c-axis texture and magnetic anisotropy, and it can be achieved by using the SPS system. Hot deformed Nd-Fe-B magnets have attracted much attention due to their good magnetic performance together with desirable thermal stability, corrosion resistance, and fracture toughness. [40]

There is a crystallographic alignment, due to the $Nd_2Fe_{14}B$ grain texture caused by the HD-process, in which the easily magnetized axis (c-axis) of the magnetic grains is aligned parallel to the pressing direction. This anisotropic behavior of the Nd-Fe-B magnet produced by hot deformation was studied [41], and the results showed that the remanence and the energy product measured in the direction parallel to the c-axis were higher than those measured in the direction perpendicular to the c-axis.

It has been proved that combining SPS process and HD process produces magnets with better magnetic properties and increased remanence compared to the SPS samples.

Liu et al. [33] also studied the influence of hot deformation on the microstructure and the magnetic properties of SPS-processed Nd-Fe-B magnets and confirmed that there is no obvious grain growth during the hot deformation process at optimum deformation temperature, and the exchange coupling is enhanced. They concluded that the HD process does not have a negative effect on the temperature stability of SPS-processed magnets.

On the contrary, according to Hou et al. [42], the relative fine and regular grain microstructure of SPS-HD-processed Nd-Fe-B magnets is beneficial in improving the temperature coefficient of coercivity.

Concerning the SPS-processed Nd-Fe-B magnets, using a low-melting-point eutectic alloy in the process was successful also for the hot deformation process. The liquid phase along grain boundaries helped to maintain the uniform microstructure. The Nd-rich phase assisted in the stress-induced grain growth, leading to the crystallographic alignment of the $Nd_2Fe_{14}B$ grains [34]. Huang et al. [43] concluded that the Nd-rich phase plays an even more important role because when there was no Nd-rich phase, no crystallographic alignment could be observed.

2.5. Grain boundary diffusion

Various low melting diffusion sources such as Nd-Cu, Nd-Al, Nd-Mn, Nd-Zn, and Nd-Ga alloys have been used for the low-melting-point diffusion process on the hot-deformed magnets [44]. The largest coercivity achieved without using heavy rare earth elements at room temperature was limited to 2.6T. A room temperature coercivity of 2.8T was reported by Seelam et al. [45] by diffusion of a Pr-based glass forming alloy into the hot-deformed Nd-Fe-B magnets. However, this coercivity enhancement was always achieved at the expense of remanence.

If the magnetic anisotropy field at the surface of the $Nd_2Fe_{14}B$ grains is higher than that inside the grains, the coercivity can be increased without a considerable reduction in remanence. In 2005, Nakamura et al. [46] reported a new method named “Grain Boundary Diffusion Process (GBDP)” in which Dy can be enriched along the grain boundaries of a Nd-Fe-B sintered magnet. The coercivity of the magnet coated with heavy rare-earth powders and then heat-treated, was enhanced significantly without a considerable reduction in remanence. [46] However, the grain boundary diffusion process cannot be applied to hot-deformed magnets since a high processing temperature of above 900°C is needed, which results in substantial grain growth in ultrafine-grained hot-deformed magnets. [47]

The enhancement of coercivity is mainly attributed to the exchange decoupling of the $Nd_2Fe_{14}B$ grains as a result of the formation of the Nd-rich intergranular phase by the infiltration of eutectic melt. The concentration of Fe in the intergranular phase is much decreased after the diffusion process, indicating that the ferromagnetism in the grain boundary phase is diluted by the infiltration or the rare-earth eutectic alloy. [48]

By diffusing $Nd_{90}Al_{10}$ alloy, Liu et al. [44] observed that a nearly complete magnetic isolation had been realized by the diffusion process. However, an enrichment of 3 at% Al in the $Nd_2Fe_{14}B$ phase reduced the Curie temperature of the magnet which led to a poor thermal stability of coercivity. They obtained good results at 200°C for the coercivity of $Nd_2Fe_{14}B$ diffused with $Nd_{70}Cu_{30}$ alloy. But this coercivity enhancement was achieved at the expense of remanence because of the large volume fraction of non-ferromagnetic intergranular phase. [44]

The formation of a heavy-rare-earth-rich shell at the surface of $Nd_2Fe_{14}B$ grains without substantial grain growth for hot-deformed samples can be achieved only with the diffusion of low-melting-point $Nd_{62}Dy_{20}Al_{18}$ [36] or $Nd_{60}Dy_{20}Cu$ [49] eutectic alloys. However, although a large coercivity of 2.8 T with remanence of 1.3 T was successfully achieved after $Nd_{62}Dy_{20}Al_{18}$ diffusion, it was found that the Dy-rich shell rarely covered the entire surface of $Nd_2Fe_{14}B$. The influence of this Dy-rich shell on magnetization reversal and coercivity is still unclear at the moment. Moreover, due to the diffusion of Al into the $Nd_2Fe_{14}B$ main phase, the thermal stability of coercivity using $Nd_{62}Dy_{20}Al_{18}$ could be inferior to that using Nd-Cu alloy. [36]

3. Experimental techniques and procedures

3.1. Sample production

3.1.1. Sample preparation

In this thesis, most samples were already prepared from other work from the research group, and the established base of samples was wide. In order to avoid wasting rare-earth materials and raw materials, only the basic samples with $Nd_2Fe_{14}B$ and α-Fe phases were prepared to have reference results with the formula $Nd_8Fe_{87}Nb_{0.5}Zr_{0.5}B_4$ and $Nd_{13.6}Fe_{73.6}Co_{6.6}B_{5.6}Ga_{0.6}$.

The raw materials with the corresponding purities used to produce the samples were Nd (99.1%), Iron (99.97%), Boron (99.5%), Niobium (99.95%), Zirconium (99.8%), Cobalt (99.95%), and Ga (99.95%). The heat treatment temperature was 973K. The weight percentages were converted from the atomic percentages as follows.

Table 3: Weight percentage for the sample $Nd_8Fe_{87}Nb_{0.5}Zr_{0.5}B_4$

Element	Nd	Fe	Nb	Zr	B
Atomic Weight	144.24	55.85	92.91	91.22	10.81
Atomic Percentage (%)	8	87	0.5	0.5	4
Weight Percentage (%)	18.77	79.03	0.76	0.74	0.70

Table 4: Weight percentage for the sample $Nd_{13.6}Fe_{73.6}Co_{6.6}B_{5.6}Ga_{0.6}$

Element	Nd	Fe	Co	B	Ga
Atomic Weight	144.24	55.85	58.93	10.81	69.72
Atomic Percentage (%)	13.6	73.6	6.6	5.6	0.6

Weight Percentage (%)	29.89	62.63	5.93	0.92	0.63

A micro-balance with a precision of 0.1mg and an error of ± 0.2mg was used to weigh the raw materials.

3.1.2. Arc melting

Arc melting is a technique used to melt metals under an electric arc that is struck by a high applied voltage. There are four main parts in an arc-melter: vacuum chamber, power supply, melting electrode with water-cooling system, and a copper support with water-cooling system as shown in Figure 14.

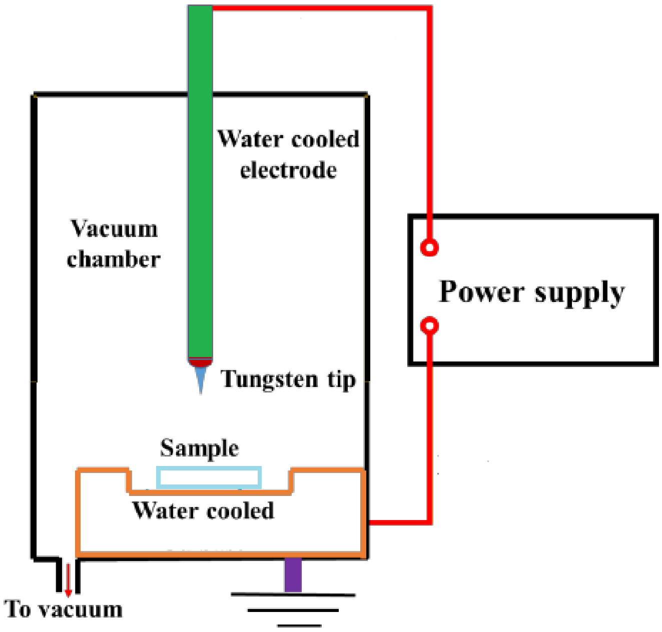

Figure 14: Schematic illustration of an arc-melter

The power supply is for two different steps: first of all, a high electrical voltage in order to initiate the electrical breakdown in the gaseous atmosphere between the electrode and the copper support, second, a high current for the melting process.

The electrode which was used was a tungsten tip held in place with a copper sleeve and fastener because the melting point of tungsten is 3422°C which is way above the melting temperature of the metals used in this study. [50]

The smaller pieces were laid underneath the larger pieces (Neodymium and Iron) to prevent them from shifting from the power of the arc-melter. The metals were heated to their melting point when the electricity passed through them. The vacuum was made in the chamber with ultra-high purity (UHP) Argon to prevent the formation of any oxides. Once the samples were in the chamber, the purging was done 5-6 times with a base pressure of 60 millitorr. A Zirconium piece was kept at a certain distance from the sample and was used as an indicator of any oxidation. This was done by checkin that there was no tarnishing after the solidification of the piece. After that, once the metals were melted in an ingot, it was flipped over and re-melted to reach homogeneity. It could be retrieved after cooling down for a few minutes.

3.1.3. Melt spinning

Melt spinning is a process used to cool molten metals very rapidly and obtain ribbons. We used the following steps as outlined:

i. We used a quartz crucible, obtained a 0.7mm orifice at the bottom, and then loaded the crucible with the sample in it inside the melt-spinning chamber with the portion of the crucible containing the ingot surrounded by a high frequency induction coil.

ii. We purged the chamber with UHP Ar by pumping down three times respectively to 4x10^{-2}, 3.5x10^{-2} and 2.3x10^{-2} torr to remove any traces of oxygen which could cause oxidation.

iii. We applied the cooling water.

iv. We rotated the wheel at the required speed: 40m/s to over-quench the sample.

v. We turned on the power supply, melted the sample for 2-3min and shot the molten sample towards the spinning wheel to form the ribbons by releasing the ballast previously pressurized at 0.2 bar and forcing the melted material onto the rotating copper wheel.

vi. We collected the ribbons.

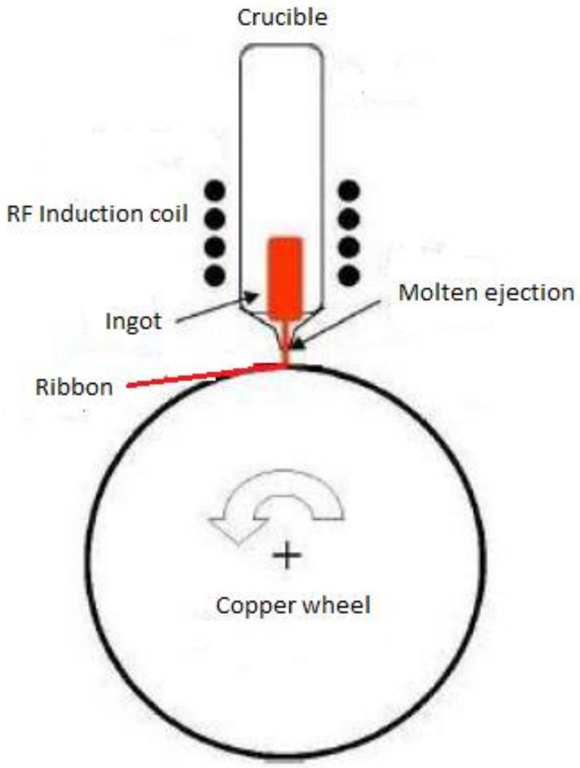

Figure 15: Schematic illustration of a melt-spinner

3.1.4. Annealing

Annealing is a heat treatment technique used to facilitate the formation of a phase, and as such, high temperatures provide energy needed for the diffusion of the atoms. The heat energy increases the diffusion rate and leads to the movement of atoms. Therefore as a result, it leads to the reduction of dislocations and stress.

The next step in the process was to anneal the sample to allow for grain growth and crystallization. In order to fully crystallize the sample, the annealing temperature had to be higher than the crystallization temperature. To prepare for annealing, the sample ribbons were placed into tantalum foil tubes. These were placed in quartz tubes and were evacuated to a pressure below 60 millitorr and refilled with Ar at least 5 times to prevent oxidation. Finally, the tubes were sealed.

The tube was placed into the furnace, which was already at the proper temperature, between 600°C and 700°C in this study, and was left for the required amount of time, 20min in this study.

3.2. Magnetic properties measurement

The characteristics of magnetic materials (saturation magnetization, coercivity, permeability) are best determined from a hysteresis loop. The most common measurement method employed for hysteresis loop determination is the vibrating sample magnetometer (VSM) while superconducting quantum interference device (SQUID) is preferred when sensitivity is required. In this study, two devices were used. A quantum design magnetic property measurement system (MPMS) SQUID with an applied field of 70kOe or 30kOe. Also, a VSM (VersaLab) with an applied field of 30kOe since we did not need to reach the saturation magnetization for the samples used.

3.2.1. Vibrating Sample Magnetometer (VSM)

VSM systems are used to measure the magnetic properties of materials as functions of magnetic field, temperature, and time. Powders, liquids, single crystals, and thin films can be used in a VSM. In this study, the VSM used was VersaLab (Quantum Design, CA, USA) and it was used at room temperature for basic references with a maximum applied field of 30 kOe. The sample was placed on a rod using non-conductive tape and then placed in the VSM chamber, surrounded by the pickup coils as shown in Figure 16. [50]

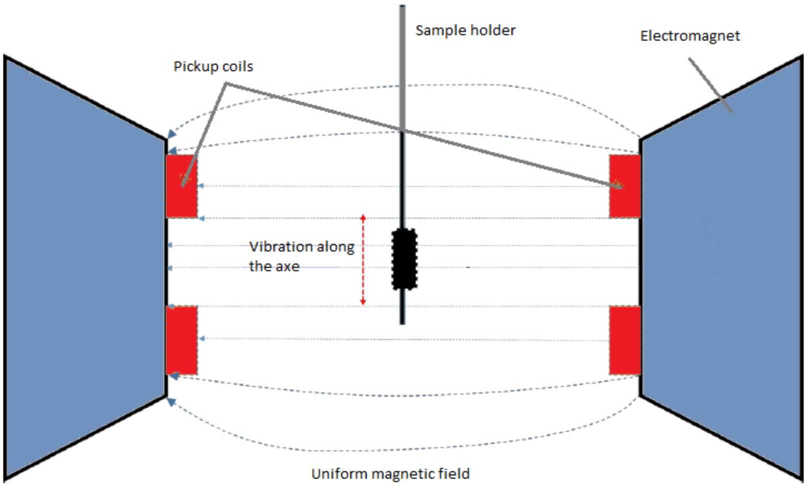

Figure 16: Schematic illustration of detection mechanism in a VSM

The rod was positioned between two electromagnets which have detection coils. The chamber was pumped down to 40 torr, the sample was magnetized to the required maximum applied field, and then the oscillation motion of the magnetized sample induced a voltage detected by the pickup coils. The induced voltage is proportional to the magnetization of the sample. The detected signals were sent to the controlling and monitoring software in the connected computer and we obtained a hysteresis loop M-H.

3.2.2. Superconducting Quantum Interference Device (SQUID)

The SQUID is one of the most sensitive experimental techniques to magnetically characterize samples with a high sensitivity (order of 10^{-9}emu).

The principle of the SQUID magnetometer is based on superconducting loops containing Josephson junctions (two superconductors separated by thin narrow insulating gaps). There are several superconducting components in a SQUID: a superconducting magnet, detection coils, flux transformer, and superconducting shields as shown in Figure 17 [50]. The sample is attached to the sample rod and is scanned through the superconducting coil, which forms a close flux transformer. Changes of the sample position cause variation of magnetic flux through the coils. The shape and magnitude of the response curve can be analyzed to obtain a corresponding magnetic moment. The magnetic field is produced by the superconducting magnet and is uniformly distributed throughout the coil area. Temperature control is conducted by placing the sample in a sealed variable temperature insert which is thermally isolated from the coil by an annular vacuum space. In our study, the maximum applied field was 70 kOe and the sample underwent a full reversal of applied field (-70 kOe) and the temperatures varied between room temperature and 200°C.

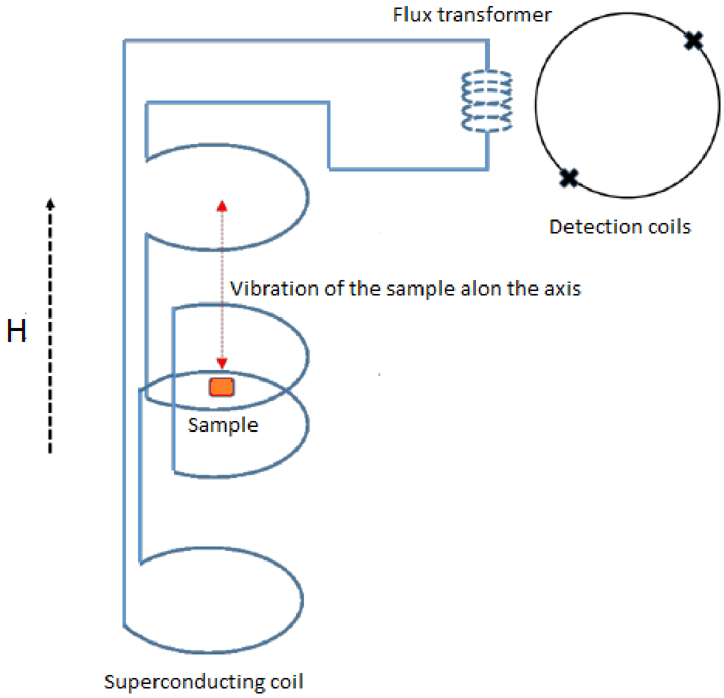

Figure 17: Schematic illustration of a SQUID magnetometer

3.2.3. Sample preparation

The sample preparation for the VSM and the SQUID were the same, except that a smaller weight was necessary for the SQUID in order to have better results. The samples were weighed using a micro-balance (±0.0001 mg).

- For annealed ribbons: small pieces of ribbons were weighed

- For SPS-processed samples: the graphite foil from the top and the bottom had already been removed by grinding and polishing. Since oxidation was not a concern for SPS samples, there was no need to produce new samples and a small piece was cut from the remaining SPS samples using a diamond saw, ground (100 grit sand paper) to a thickness of about 200 µm and then polished (800 grit sand paper). To finish, the sample was rinsed with acetone and weighed.
- For the HD sample and the GBD sample: samples were already prepared and not oxidized, so only the rinse was needed before measuring the weight.

Only annealed samples were used on the VSM before its software failure and then the SQUID was used. For the rest of the samples, only the direction along the pressing and deforming direction were measured. The samples were taped in a small piece of plastic cut from a straw with non-conductive tape for the VSM, or taped on a support for the SQUID, then placed inside a plastic straw and inside the chamber for measurement.

4. Results and Discussion

4.1. Data conversion and characterization

Both the VSM Versa Lab and the SQUID yielded results as follows: the magnetic field in Oersted and the magnetic moment in emu. The magnetization is used in emu/g, which needs to be converted to emu/cm^3 when calculating the flux density and energy product. The density of the sample that we used to convert the unit is 7.6

g/cm^3. In some results and discussion, the Tesla unit is used for the magnetic field, which can be converted from Oe as follows: 1 [Oe] = 0.0001 [T].

The thermal stability of the samples was also analyzed, more precisely the effect of temperature ($T_{RT} – T_T$) on coercivity and remanence. This effect can be characterized with:

The temperature coefficient of remanence - α in %/°C between room temperature and a chosen temperature:

$$\alpha = \frac{B_r(T_{RT}) - B_r(T_T)}{B_r(T_{RT})(T_T - T_{RT})} \text{x}100$$

where B_r is the remanence, T_{RT} the room temperature, T_T the chosen temperature. The temperature coefficient of coercivity - β in %/°C between room temperature and a chosen temperature:

$$\beta = \frac{H_c(T_{RT}) - H_c(T_T)}{H_c(T_{RT})(T_T - T_{RT})} \text{x}100$$

where H_c is the coercivity, T_{RT} the room temperature, and T_T the chosen temperature.

For the rest of the study, in order to obtain representative results, a margin of error of ±0.003 will be considered for α and β values. For coercivity and remanence values, a margin of error of ±50 and ±0.2 respectively.

4.2. Melt-spinning and annealing

4.2.1. Basic compositions $Nd_8Fe_{87}Nb_{0.5}Zr_{0.5}B_4$ and $Nd_{13.6}Fe_{73.6}Co_{6.6}B_{5.6}Ga_{0.6}$

As determined by Y. Lin [51], the optimum annealing temperature for Nd-Fe-B magnets ($Nd_8Fe_{87}Nb_{0.5}Zr_{0.5}B_4$) is 700°C and the optimum annealing time is 20 minutes. When the temperature was under 700°C or the time was less than 20min, the crystallization of $Nd_2Fe_{14}B$ phase was not fully realized and the amorphous phase still existed in the samples. When the temperature was higher than 700°C or the time was more than 20 minutes, excessive grain growth happened. [51]

Concerning the $Nd_{13.6}Fe_{73.6}Co_{6.6}B_{5.6}Ga_{0.6}$ samples, as determined by L. Zhang, [37] the optimum annealing temperature is around 630°C and the optimum annealing time is 20 minutes. At this temperature, the grain size is about 30-45 nm which is good for further SPS processing. Above 640°C, the grain size is about 50-350 nm which is not suitable for further SPS processing and below 620°C, the presence of the amorphous phase is a concern.

For the purpose of this study, $Nd_8Fe_{87}Nb_{0.5}Zr_{0.5}B_4$ samples were produced and annealed at 700 °C for 20 minutes, as well as $Nd_{13.6}Fe_{73.6}Co_{6.6}B_{5.6}Ga_{0.6}$ samples annealed at 630°C for 20 minutes. They serve as a base for comparison of further results.

Figure 18 shows the half-hysteresis loop at room temperature of the $Nd_8Fe_{87}Nb_{0.5}Zr_{0.5}B_4$ sample and Figure 19 shows the half-hysteresis loop at room temperature of the $Nd_{13.6}Fe_{73.6}Co_{6.6}B_{5.6}Ga_{0.6}$ sample.

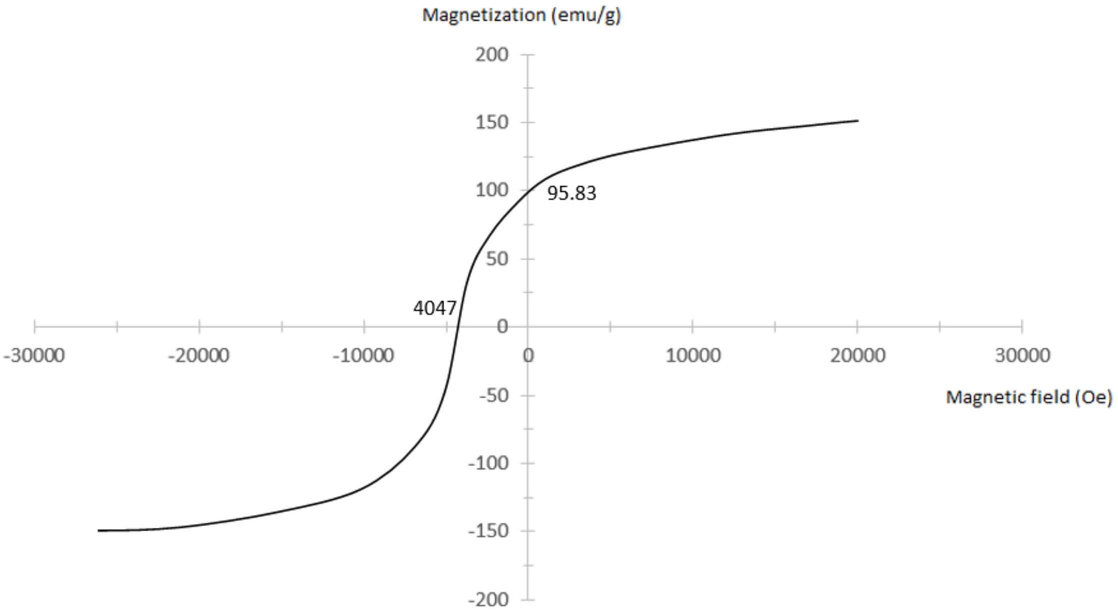

Figure 18: Half-hysteresis loop of $Nd_8Fe_{87}Nb_{0.5}Zr_{0.5}B_4$ at room temperature after annealing at 700°C for 20 min

The remanence, coercivity and energy product are 95.83 emu/g, 4047 Oe and 10.04 MGOe respectively for the $Nd_8Fe_{87}Nb_{0.5}Zr_{0.5}B_4$ sample.

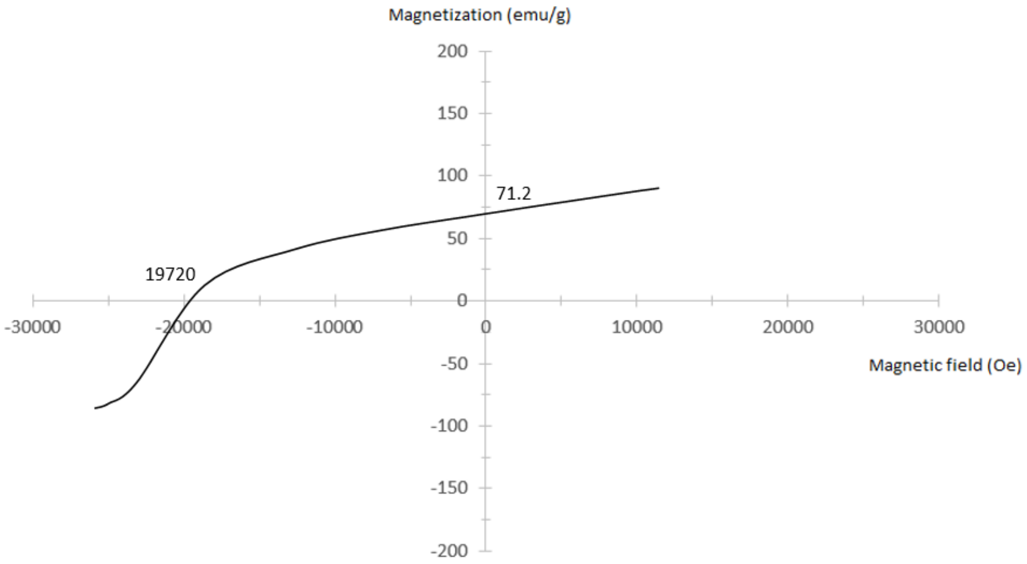

Figure 19: Half-hysteresis loop of $Nd_{13.6}Fe_{73.6}Co_{6.6}B_{5.6}Ga_{0.6}$ at room temperature after annealing at 630°C for 20 min

The remanence, coercivity and energy product were 71.2 emu/g, 19720 Oe, and 10.03 MGOe, respectively, for the $Nd_{13.6}Fe_{73.6}Co_{6.6}B_{5.6}Ga_{0.6}$ sample.

The values of coercivity and remanence were analyzed from 20°C up to 200°C for both samples and the results are shown in Figure 20 and Figure 21.

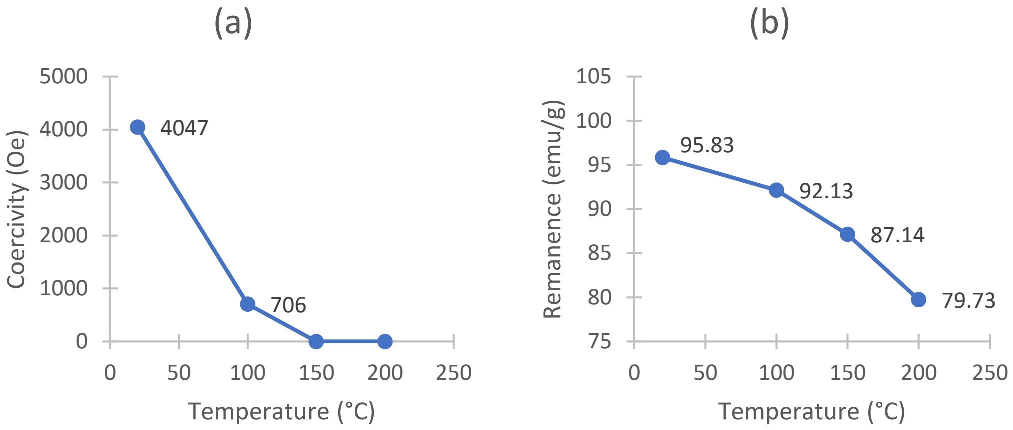

Figure 20: Coercivity (a) and remanence (b) values of $Nd_8Fe_{87}Nb_{0.5}Zr_{0.5}B_4$ from 20°C up to 200°C after annealing at 700°C for 20 min

For $Nd_8Fe_{87}Nb_{0.5}Zr_{0.5}B_4$, the coercivity dropped drastically between room temperature (RT) and 200°C; in this case, the temperature coefficient of coercivity between 20-100°C reached -1.032%/°C. The use of permanent magnets at elevated temperature is directly linked to thermal stability and more precisely to the thermal stability of coercivity. Therefore, for the rest of this study, the samples based on this composition were studied between RT and 100°C as a maximal temperature to observe their respective behaviors under higher temperatures and obtain elements that can be representative.

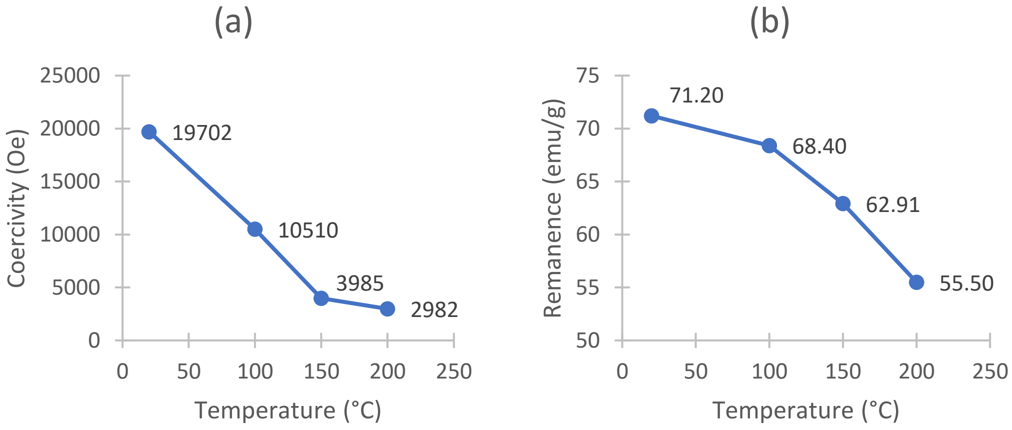

Figure 21: Coercivity (a) and remanence (b) values of $Nd_{13.6}Fe_{73.6}Co_{6.6}B_{5.6}Ga_{0.6}$ *from 20°C up to 200°C after annealing at 630°C for 20 min*

The higher Nd content of $Nd_{13.6}Fe_{73.6}Co_{6.6}B_{5.6}Ga_{0.6}$ and the lower annealing temperature played a role in separating the $Nd_2Fe_{14}B$ grains with the Nd-rich intergranular phase, leading to a better coercivity. In that case, the temperature coefficient of coercivity was -0.471%/°C between 20-200°C.

For comparison, for $Nd_{13.5}Fe_{80.5}B_6$ between 300-400K (26-126°C), S. Ur-Rheman et al. [52] obtained a coercivity coefficient of -0.41%/°C. At room temperature, the coercivity was about 13823 Oe. However, above 400K, the coercivity dropped drastically. Thus, the room temperature coercivity and the thermal stability of the $Nd_{13.6}Fe_{73.6}Co_{6.6}B_{5.6}Ga_{0.6}$ sample between 20-200°C seem promising.

The Ga addition improved coercivity for two reasons. First, it increased uniaxial anisotropy due to Ga non-magnetic atoms entering the hard phase $Nd_2Fe_{14}B$ to substitute for Fe and therefore enhancing the coercivity of the magnet. Second, it formed Nd-rich intergranular phases containing Ga, which more effectively separated the magnetic grains and weakened the exchange-coupled demagnetization effect. [23]

4.2.2. Effects of Dy addition

Different magnets with increasing content of Dy were analyzed at an annealing temperature of 620°C:

- $((Nd_{0.9}Dy_{0.1})_{15}Fe_{77}B_8)_{99}S_1$
- $((Nd_{0.8}Dy_{0.2})_{15}Fe_{77}B_8)_{99}S_1$
- $((Nd_{0.7}Dy_{0.3})_{15}Fe_{77}B_8)_{99}S_1$

The samples did not show any exterior sign of oxidation, which was a concern in the case of ribbons. They were stored in a protective gas environment. The background of these samples listed no previous thermal analysis and no destructive analysis techniques. Therefore, the melt-spun ribbons were usable for thermal analysis.

The magnetic properties of the samples were studied from 20°C up to 200°C as shown in Figure 22, Figure 23, and Figure 24.

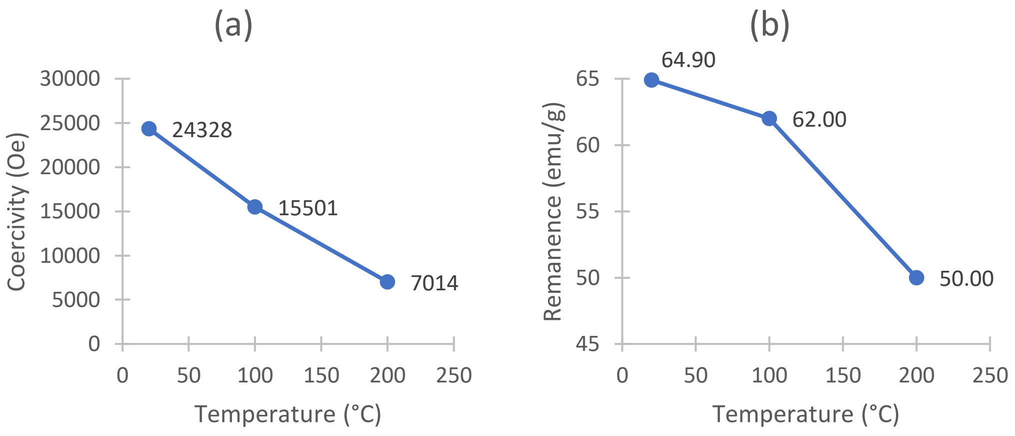

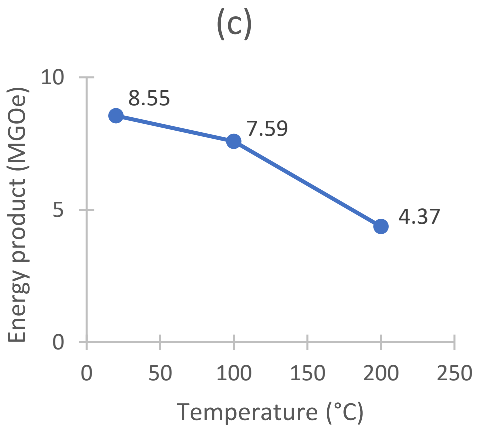

Figure 22: Coercivity (a), remanence (b) and energy product (c) respective values of $((Nd_{0.9}Dy_{0.1})_{15}Fe_{77}B_8)_{99}S_1$ from 20°C up to 200°C after annealing at 620°C for 20 min

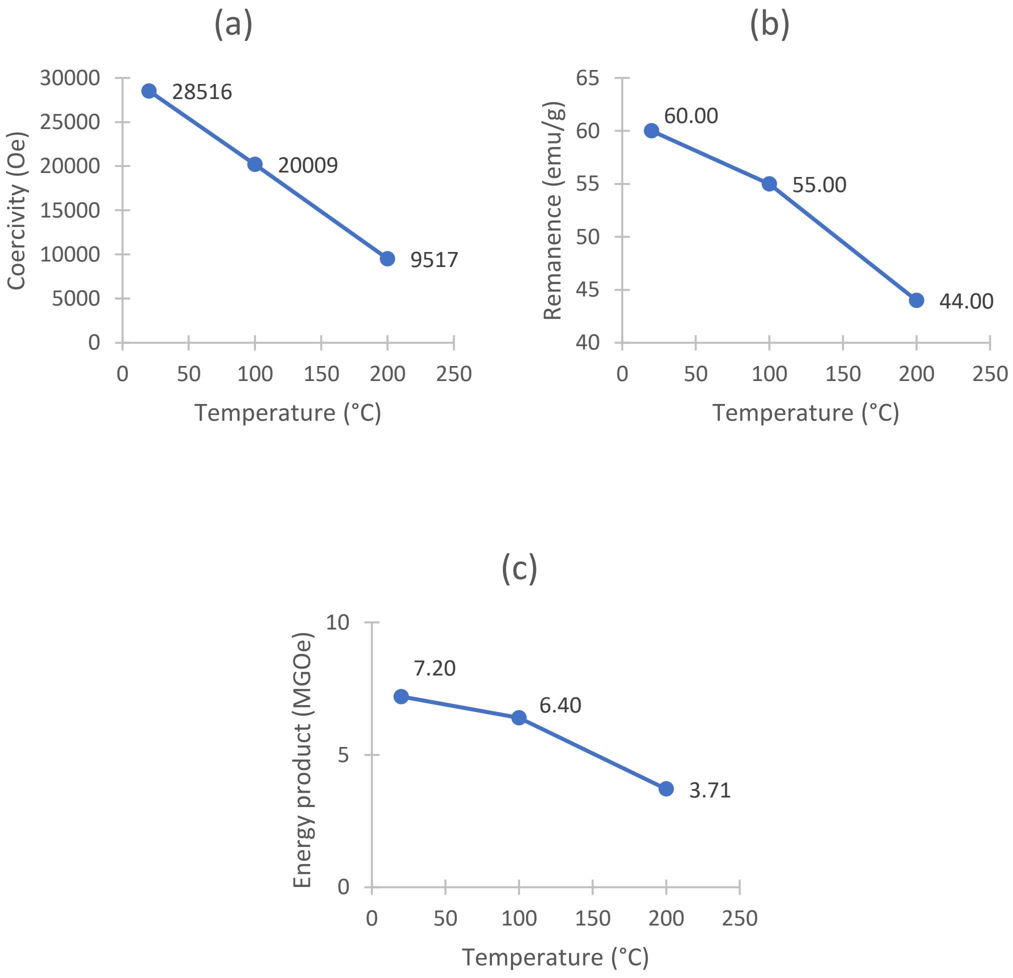

Figure 23: Coercivity (a), remanence (b) and energy product (c) respective values of $((Nd_{0.8}Dy_{0.2})_{15}Fe_{77}B_8)_{99}S_1$ from 20°C up to 200°C after annealing at 620°C for 20 min

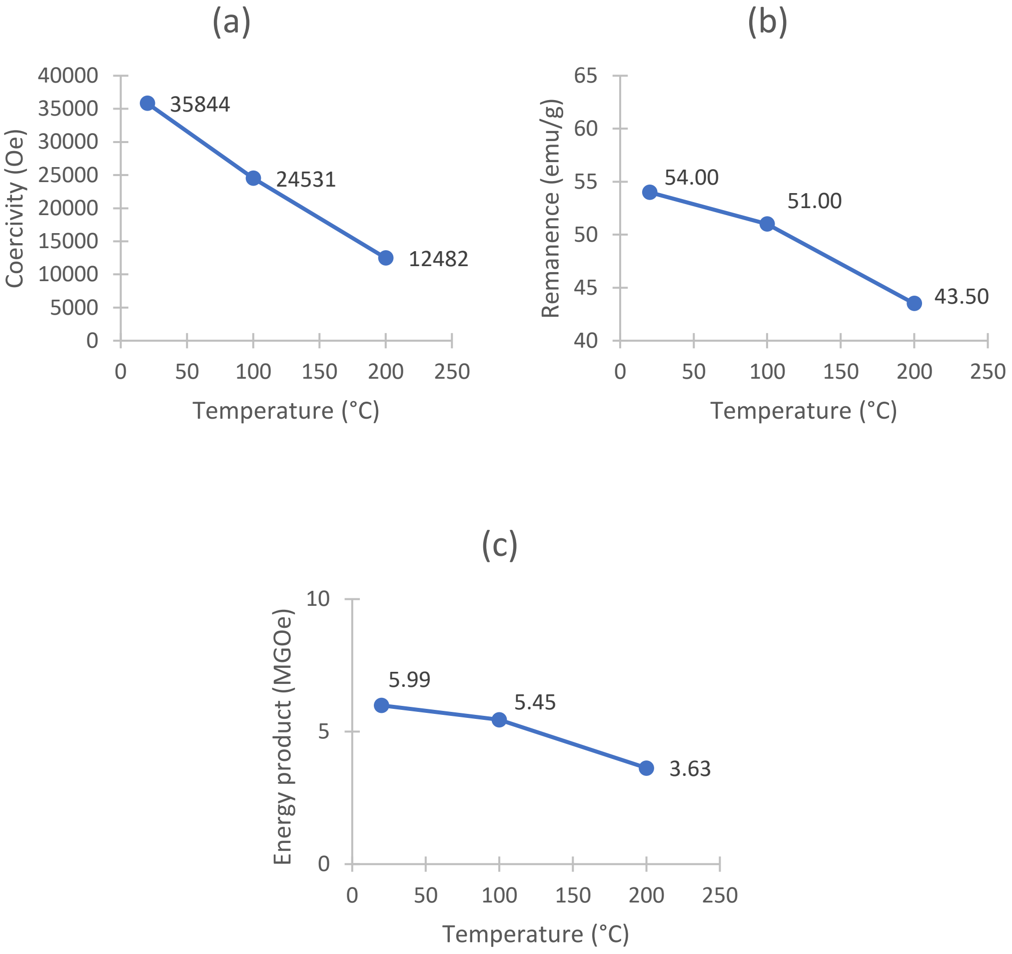

Figure 24: Coercivity (a), remanence (b) and energy product (c) respective values of $((Nd_{0.7}Dy_{0.3})_{15}Fe_{77}B_8)_{99}S_1$ from 20°C up to 200°C after annealing at 620°C for 20 min

The temperature coefficient of coercivity between 20-200°C, depending on the Dy atomic percentage, is listed in Table 5. It shows that Dy is an effective element to enhance coercivity by increasing magnetocrystalline anisotropy, reducing the average grain size, and improving the thermal stability.

Table 5: Temperature coefficient of coercivity between 20-200°C of samples with different Dy content annealed at 620°C for 20 min

Dy atomic percentage (at.%)	**Temperature coefficient of coercivity**
1.5	-0.395%/°C
3	-0.370%/°C
4.5	-0.362%/°C

To obtain a coercivity above 2.5T at room temperature, the Dy content has to be above 1.5 at.%.

New samples of melt-spun ribbons were analyzed in order to observe the effects of combined additions of Dy, Co, and Ga and the behavior of magnetic properties in relation with the temperature. The background of the samples was the same as the previous samples with Dy content.

- $Nd_{13}Dy_2Fe_{72.2}Co_{6.6}B_{5.6}Ga_{0.6}$ annealed at 610°C
- $Nd_{13}Dy_2Fe_{72.2}Co_{6.6}B_{5.6}Ga_{0.6}$ annealed at 630°C
- $Nd_{13}Dy_2Fe_{72.2}Co_{6.6}B_{5.6}Ga_{0.6}$ annealed at 650°C

The sample with the highest coercivity was the sample annealed at 650°C with a coercivity of 27.2 kOe. However, the sample with the best coercivity stability over an increasing temperature was the sample annealed at 610°C. This was mostly likely due to the grain size, which increased as the annealing temperature increased. Its magnetic properties are shown in Figure 25.

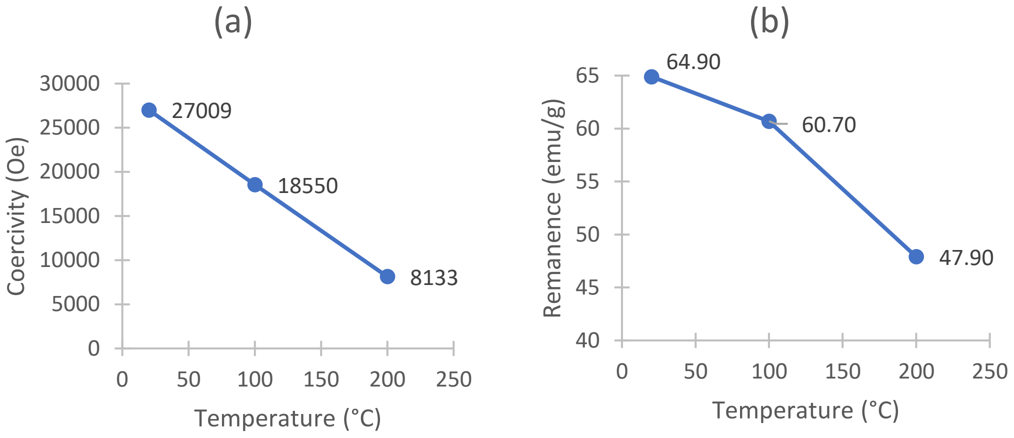

Figure 25: Coercivity (a) and remanence (b) values of $Nd_{13}Dy_2Fe_{72.2}Co_{6.6}B_{5.6}Ga_{0.6}$ *from 20°C up to 200°C, after annealing at 610°C for 20 min*

The combination of Dy, Co, and Ga with a 0.2 atomic percentage of Dy resulted in a temperature coefficient of coercivity of -0.388%/°C with an annealing at 610°C.

Besides, the combination of Co, Ga, and Dy elements led to better magnetic properties, higher energy product (8.76 MGOe at RT) and remanence (64.9 KOe at RT), than the samples with only the Dy addition and a room temperature coercivity above 2.5 T. At 200°C, the sample still maintained better magnetic properties than the others two with an energy product of 5.11 MGOe.

4.3. Spark Plasma Sintering (SPS)

Concerning all samples which had been SPS processed, only the magnetic properties in the direction parallel to the sintering direction of SPS-processed samples were measured because the parallel direction was easier to magnetize than the perpendicular direction. This is related to the crystallographic alignment which occurs during the SPS process as previously discussed.

4.3.1. Basic composition samples $Nd_8Fe_{87}Nb_{0.5}Zr_{0.}5B_4$ and $Nd_{13.6}Fe_{73.6}Co_{6.6}B_{5.6}Ga_{0.6}$ after SPS processing

It can be seen that the use of the SPS process on the $Nd_8Fe_{87}Nb_{0.5}Zr_{0.5}B_4$ sample (background of this sample was a heating rate of 100°C/min with sintering temperature 700°C and sintering pressure 100MPa) led to a high decrease of coercivity, a small decrease of remanence, and therefore of energy product, compared to the melt-spun ribbons (coercivity 4047 Oe, remanence 95.83 emu/g). No low-melting-point alloy was used so we could observe the impact of the SPS process without it. The main problem was the drastic decrease of coercivity, reaching a zero value above 50°C as shown in Figure 26.

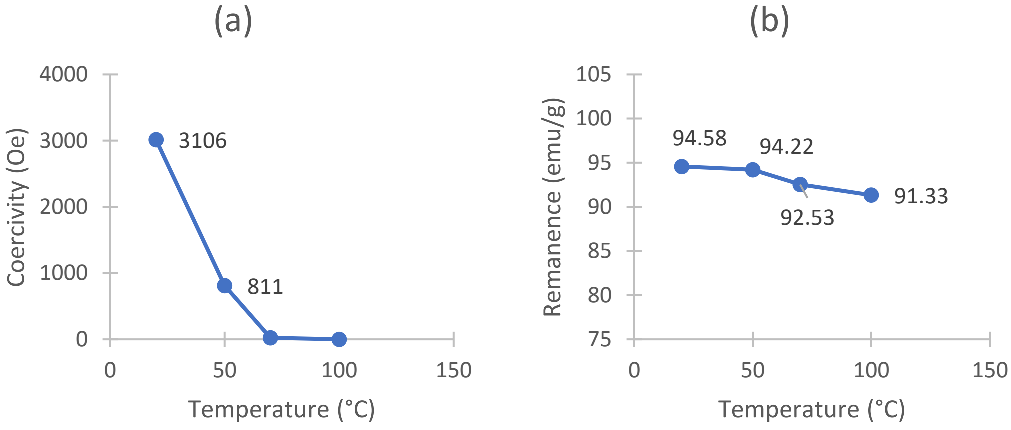

Figure 26: Coercivity (a) and remanence (b) values of $Nd_8Fe_{87}Nb_{0.5}Zr_{0.5}B_4$ from 20°C up to 100°C after SPS processing at 700°C

Concerning the basic composition $Nd_{13.6}Fe_{73.6}Co_{6.6}B_{5.6}Ga_{0.6}$ (background of this sample was a heating rate of 10°C/min with sintering temperature 700°C and sintering pressure 100MPa), a decrease of coercivity also occurred, but due to the higher amount of Nd originally present, it was less critical. Results are shown in

Figure 27. Moreover, the coercivity temperature coefficient between 20-200°C is also decreased to -0.490%/°C instead of -0.471%/°C for the melt spun ribbons.

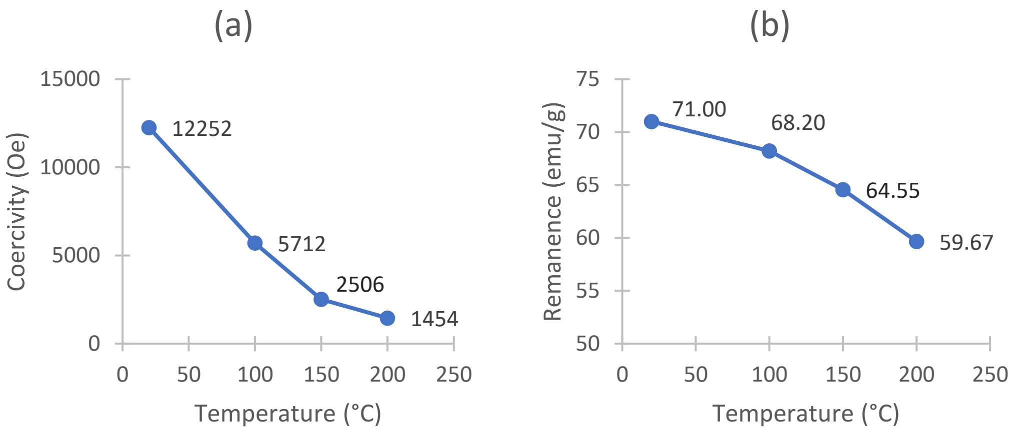

Figure 27: Coercivity (a) and remanence (b) values of $Nd_{13.6}Fe_{73.6}Co_{6.6}B_{5.6}Ga_{0.6}$ from 20°C up to 200°C after SPS processing at 700°C

The decrease of the coercivity is linked to the microstructure of the sample: the more uniform the microstructure is, the higher coercivity will be. During the SPS process, the localized high heating led to an uneven grain growth and a loss of uniformity in the microstructure as previously mentioned. It is believed that the temperature at the surface may reach the boiling point of the material and hence nano-sized grains recrystallize into micro-sized grains during cooling. [53]

Grain growth, however, has an important impact concerning the thermal stability of the sample. Reducing it means having a better thermal coefficient of coercivity and remanence. To reduce the grain growth, low-melting-point alloys such as $Nd_{70}Cu_{30}$ or $Pr_{68}Cu_{25}Al_7$ were used during the SPS process.

4.3.2. Addition of 5wt.% $Nd_{70}Cu_{30}$ during SPS processing

For this study, 5wt.% $Nd_{70}Cu_{30}$ was added to two different samples: $Nd_8Fe_{87}Nb_{0.5}Zr_{0.5}B_4$ and $Nd_7Dy_1Fe_{87}Nb_{0.5}Zr_{0.5}B_4$. The results obtained are shown respectively in Figure 28 and Figure 29.

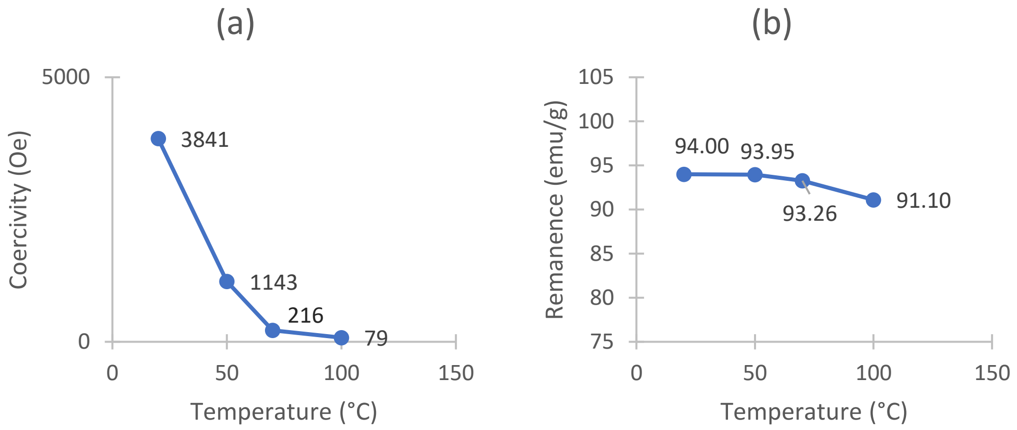

Figure 28: Coercivity (a) and remanence (b) values of $Nd_8Fe_{87}Nb_{0.5}Zr_{0.5}B_4$ with 5wt.% $Nd_{70}Cu_{30}$ from 20°C up to 100°C after SPS processing at 700°C

This time, we obtained, at 100°C, a non-zero measurement of coercivity. The coercivity temperature coefficient was -1.224%/°C between 20-100°C.

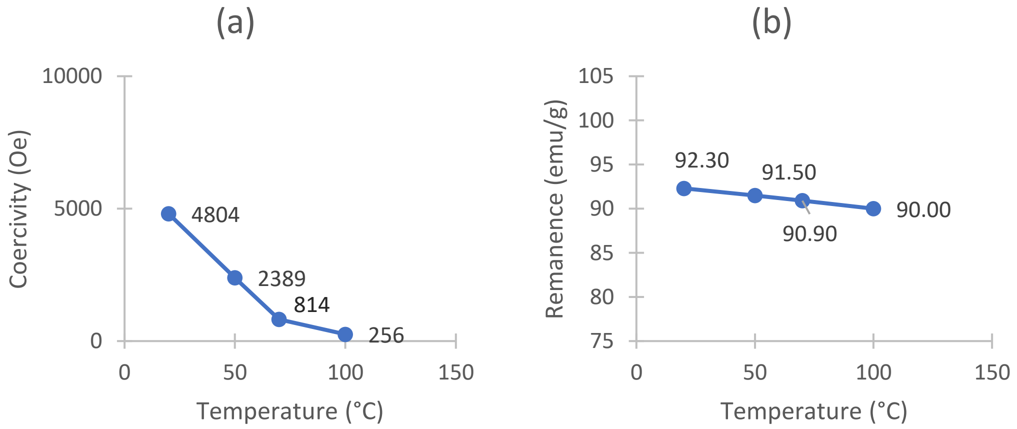

Figure 29: Coercivity (a) and remanence (b) values of $Nd_7Dy_1Fe_{87}Nb_{0.5}Zr_{0.5}B_4$ with 5wt.% $Nd_{70}Cu_{30}$ from 20°C up to 100°C after SPS processing at 700°C

In that case, we also obtained a non-zero measurement of coercivity at 100°C. The coercivity temperature coefficient was -1.183%/°C between 20-100°C.

The low-melting-point alloy diffused along the grain boundary phase during the SPS process and assisted in maintaining the uniform microstructure as well as isolating the $Nd_2Fe_{14}B$ grains, which is why the decrease of coercivity was reduced.

We can observe that the addition of Dy had a considerable impact on the thermal stability and the coercivity of the melt-spun sample compared to its impact on the SPS-processed sample. The coercivity at room temperature of the melt-spun sample was increased by 27% instead of 20% for the SPS-processed sample. Moreover, the coercivity coefficient of temperature of the melt-spun sample has improved more than that of the SPS-processed sample.

Therefore, Nd-Fe-B melt-spun magnets might be considered more dependent on heavy rare-earth elements for high-temperature performance than the alternative spark plasma sintered Nd-Fe-B magnets.

4.3.3. Addition of 10w.% $Pr_{68}Cu_{25}Al_7$ with $Nd_{13.6}Fe_{73.6}Co_{6.6}B_{5.6}Ga_{0.6}$ during SPS processing

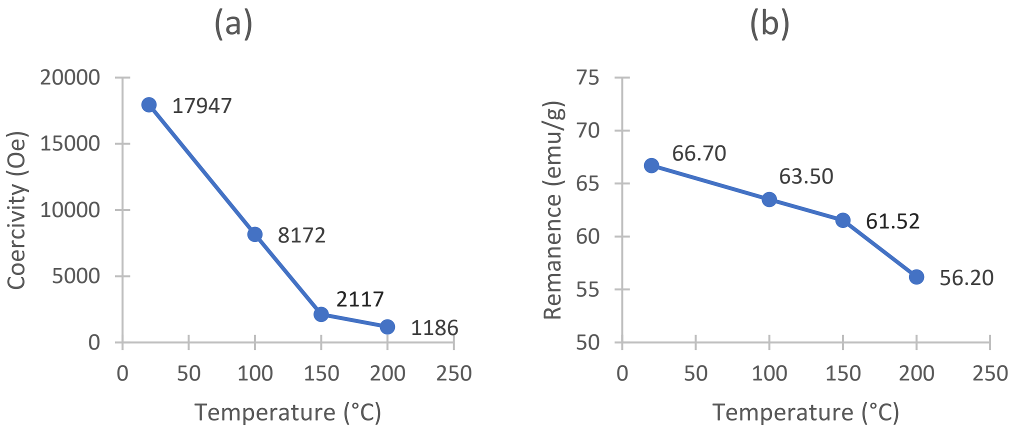

Figure 30: Coercivity (a) and remanence (b) values of $Nd_{13.6}Fe_{73.6}Co_{6.6}B_{5.6}Ga_{0.6}$ with 10w.% $Pr_{68}Cu_{25}Al_7$ from 20°C up to 200°C after SPS processing at 700°C

The coercivity of the SPS sample without the addition of the low-melting-point alloy is was lower than that of the melt-spun ribbons. In previous studies, this had been linked to the formation of coarse grain zones. By adding the $Pr_{68}Cu_{25}Al_7$, the coarse grain zones were suppressed [37]. However, there was a decrease in remanence due to the magnetic dilution effect because the $Pr_{68}Cu_{25}Al_7$ is a non-ferromagnetic material.

The $Pr_{68}Cu_{25}Al_7$ powders were melted during the SPS process, and the liquid infiltrated into the powder particle void space and grain boundaries. This led to the formation of a low-melting-point boundary phase which inhibited growth of $Nd_2Fe_{14}B$.

Concerning the sample $Nd_{13.6}Fe_{73.6}Co_{6.6}B_{5.6}Ga_{0.6}$ with the addition of 10w.% $Pr_{68}Cu_{25}Al_7$, at a higher temperature (200°C), we can observe that coercivity decreased even faster than with the sample without the addition of $Pr_{68}Cu_{25}Al_7$, despite the fact that this sample had better results at room temperature and moderated temperatures. Moreover, in this case, the remanence was affected by the SPS process and decreased by 6%. The decrease of thermal stability and remanence are related partly to the dissolution of Al in the $Nd_2Fe_{14}B$ phase.

4.3.4. Comparative data

The comparative data for SPS-processed samples can be found in Table 6. The samples compared in this table are the following ones: The basic composition $Nd_8Fe_{87}Nb_{0.5}Zr_{0.5}B_4$ was SPS-processed, then SPS-processed with the addition of 5wt.% $Nd_{70}Cu_{30}$. Same goes for the basic composition $Nd_{13.6}Fe_{73.6}Co_{6.6}B_{5.6}Ga_{0.6}$ that was SPS-processed, then SPS-processed with the addition of 10w.% $Pr_{68}Cu_{25}Al_7$.

Table 6: Comparative data of SPS-processed samples

		$Nd_8Fe_{87}Nb_{0.5}Zr_{0.5}B_4$		$Nd_{13.6}Fe_{73.6}Co_{6.6}B_{5.6}Ga_{0.6}$	
Before SPS	Coercivity (Oe) at RT	4047		19702	
	Remanence (emu/g) at RT	95.83		71.20	
	Coercivity temperature coefficient (20-100°C)	-1.032%/°C		-0.583%/°C	
	Coercivity temperature coefficient (20-200°C)	N/A		-0.471%/°C	
		No addition	Addition of 5wt.% $Nd_{70}Cu_{30}$	No addition	Addition of 10w.% $Pr_{68}Cu_{25}Al_7$
After SPS	Coercivity (Oe) at RT	3106	3841	12252	17947
	Remanence (emu/g) at RT	94.58	94.00	71.00	66.70
	Coercivity loss at RT	-23%	-5%	-38%	-9%
	Remanence loss at RT	-2%	-2%	-1%	-6%
	Coercivity temperature coefficient (20-100°C)	N/A	-1.224%/°C	-0.667%/°C	-0.680%/°C
	Coercivity temperature coefficient (20-200°C)	N/A	N/A	-0.490%/°C	-0.519%/°C

As previously discussed, the SPS process led to a high decrease of coercivity at room temperature and, in addition, to a decrease of the thermal stability of SPS-processed samples compared to melt-spun samples of the same composition. This decrease of the thermal stability is even higher in the first hundred degrees for the SPS-processed samples compared to the melt-spun samples. The remanence of the samples without addition of low-melting-point alloy was not affected by the SPS process.

With the addition of 5wt.% $Nd_{70}Cu_{30}$, we can conclude that using this low-melting-point alloys helped improve the thermal stability and reduced the coercivity loss of the SPS-processed samples compared to the samples without it. Concerning the addition of 10w.% $Pr_{68}Cu_{25}Al_7$, it reduced the coercivity loss but had a bad impact on the thermal stability and the remanence due partly to the dissolution of Al in the $Nd_2Fe_{14}B$ phase.

The results of the SPS-processed samples with or without addition of low-melting-point alloy were still less promising than the one of the melt-spun samples. Therefore, SPS process does not seem to be suitable in order to improve the thermal stability of the samples, even with low-melting-point alloy addition.

4.4. Hot deformation

In hot-deformed samples, there is a crystallographic alignment of grains creating magnetic anisotropy, which increases the remanence. However, grain growth occurs which reduces the coercivity. The interesting part is to find out to what extent it does reduce the coercivity, and the impact it has on the thermal stability of the sample. The crystallographic alignment of most $Nd_2Fe_{14}B$ grains is in the deforming direction; it is a stress-induced preferential grain growth. This degree of alignment is higher than the one obtained after SPS processing.

The hot deformation process was the same as the sintering process except that the program was modified to change the heating rate to 200°C/min, the deforming temperature was still 700°C, the deforming pressure was 65MPa and the holding time was 10s.

4.4.1. Basic composition samples $Nd_{13.6}Fe_{73.6}Co_{6.6}B_{5.6}Ga_{0.6}$ after hot deformation at 700°C

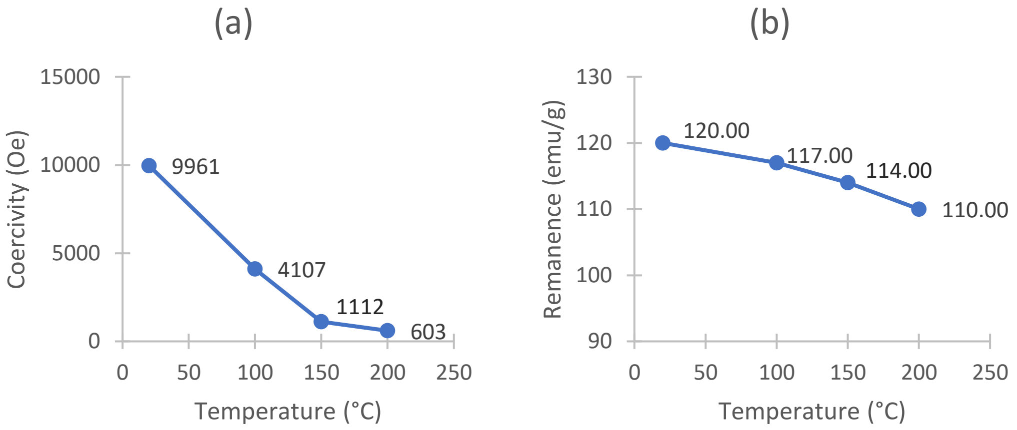

Figure 31: Coercivity (a) and remanence (b) values of $Nd_{13.6}Fe_{73.6}Co_{6.6}B_{5.6}Ga_{0.6}$ *from 20°C up to 200°C after hot deformation at 700°C*

The hot deformation process increased the remanence of the sample to 120 emu/g at room temperature but significantly decreased the coercivity from 19702 Oe for the melt-spun sample to 9961 Oe. Moreover, the coercivity temperature coefficient between 20-200°C reached -0.522%/°C instead of -0.471%/°C for the melt-spun sample of the same composition. In that case, the hot deformation process does not seem suitable at all.

4.4.2. Hot deformation applied on samples with 5wt.% $Nd_{70}Cu_{30}$ content

The mixed low-melting-point alloy melted and diffused along grain boundaries to form a liquid Nd-rich grain boundary phase which also lubricated the $Nd_2Fe_{14}B$ grains and facilitated the mass transport with the help of the pressure to align the c-axis of the $Nd_2Fe_{14}B$ grains to the deformation direction.

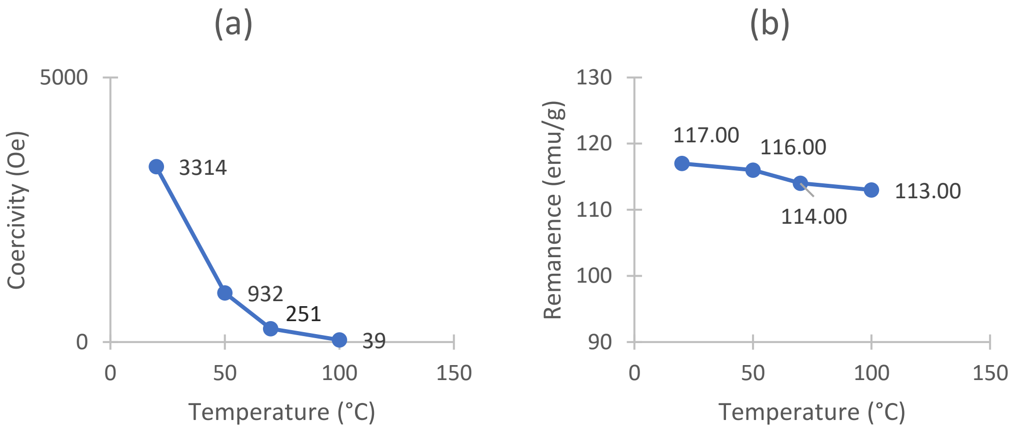

Figure 32: Coercivity (a) and remanence (b) values of $Nd_8Fe_{87}Nb_{0.5}Zr_{0.5}B_4$ with 5wt.% $Nd_{70}Cu_{30}$ from 20°C up to 100°C

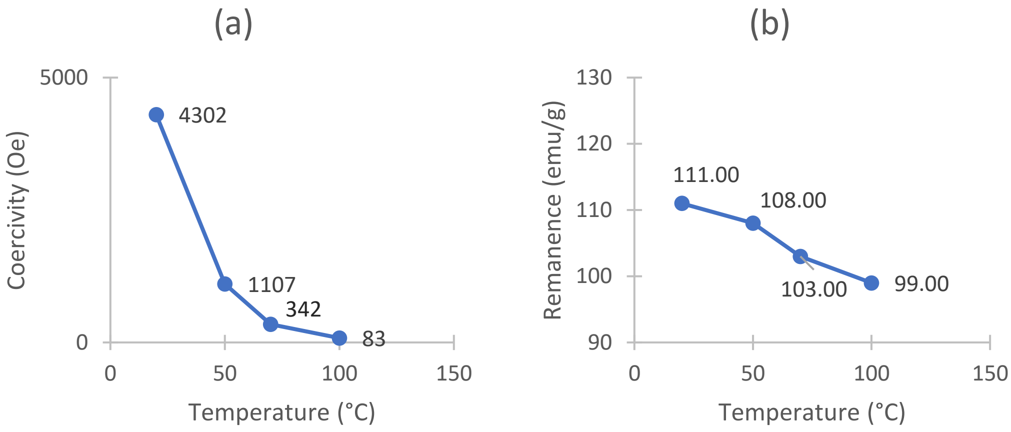

Figure 33: Coercivity (a) and remanence (b) values of $Nd_7Dy_1Fe_{87}Nb_{0.5}Zr_{0.5}B_4$ with 5wt.% $Nd_{70}Cu_{30}$ from 20°C up to 100°C

We can observe that the coercivity of both samples decreased after the hot deformation. This was mainly due to the non-uniform grain growth creating a grain size distribution, and therefore a heterogeneous microstructure. This is directly related to the nucleation of the reverse domains and to the fact that wall pinning at the grain boundaries is dominant. Another reason for the coercivity decrease is the exchange coupling between the soft and hard magnetic phase. Also, the soft magnetic phase might have increased in scale so the exchange coupling is not as good as before.

For both samples, the coercivity temperature coefficients were -1.235%/°C and -1.226%/°C, respectively between 20-100°C. The values after the SPS process were -1.224%/°C and -1.183%/°C, respectively.

4.4.3. Hot deformation applied on $Nd_{13.6}Fe_{73.6}Co_{6.6}B_{5.6}Ga_{0.6}$ with 10w.% $Pr_{68}Cu_{25}Al_7$ content

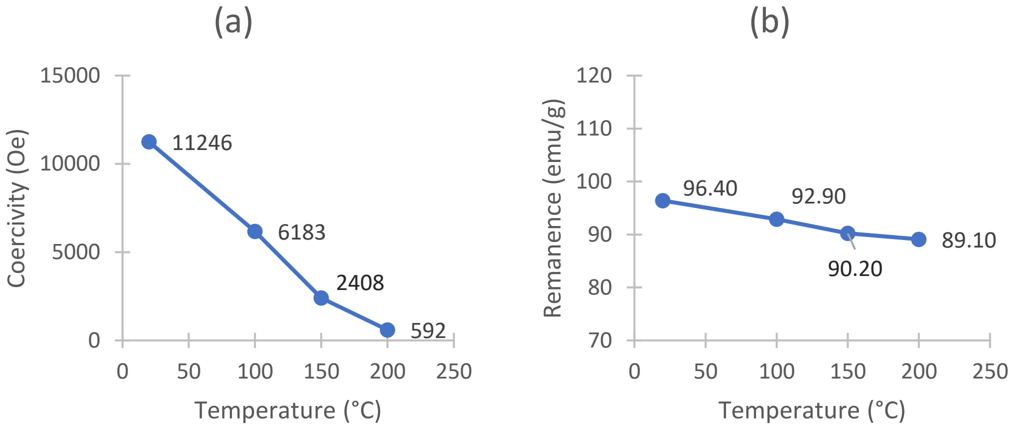

Figure 34: Coercivity (a) and remanence (b) values of $Nd_{13.6}Fe_{73.6}Co_{6.6}B_{5.6}Ga_{0.6}$ *with 10w.%* $Pr_{68}Cu_{25}Al_{7}$ *from 20°C up to 200°C*

It is proven that hot deformation, more especially the elevated temperatures needed to hot deform a sample, causes grain growth but also redistribution of rare earth elements from intergranular phases to triple-junction phases. [54] The reduction of coercivity after hot deformation could be related to the fact that the Pr and Nd elements aggregated at the triple-junction phases, which decreased the amount of intergranular phase and thus increased magnetostatic interactions. Once again, the magnetic dilution effect is at play and reduces the remanence of the sample.

In that case, we can also observe that the coercivity temperature coefficient between 20-100°C is -0.526%/°C after hot deformation instead of -0.519%/°C after SPS-process. Therefore, considering our ±0.003 error margin, the HD process does not seem to affect thermal stability compared to thermal stability of the SPS-processed samples.

4.4.4. Discussion

The coercivity of the samples is significantly lower after HD process compared to the coercivity of the melt-spun samples, even compared to the coercivity of the SPS-processed samples. This may be caused by ferromagnetic intergranular phases, surface defects, etc., which limit the enhancement of the coercivity for hot-deformed magnets. Moreover, the thermal stability was not improved by the hot deformation process.

Therefore, applying hot deformation to a sample is not fit for high-temperature application magnets.

4.5. Grain Boundary Diffusion (GBD)

The low-melting-point alloys used to coat the SPS or SPS+HD samples were used with the following amount: 20 wt.% of the sample. The samples with $Nd_{70}Cu_{30}$ or $Pr_{68}Cu_{25}Al_{7}$ applied with GBD were treated at 650°C for 2 hours and the samples with $Nd_{62}Dy_{20}Al_{18}$ at 700°C for 1 hour.

With grain boundary diffusion, sintered bodies are coated with the compounds and then heat-treated at a lower temperature than the sintering temperature. Hence, the amount diffused into the magnet is more appropriate and more efficient. This is especially important in the cases using rare-earth compound to allow a more efficient usage.

4.5.1. Grain boundary diffusion process applied to $Nd_{13.6}Fe_{73.6}Co_{6.6}B_{5.6}Ga_{0.6}$ with $Nd_{70}Cu_{30}$

For the following results shown in Figure 35, the sample was only SPS processed. No hot deformation was applied.

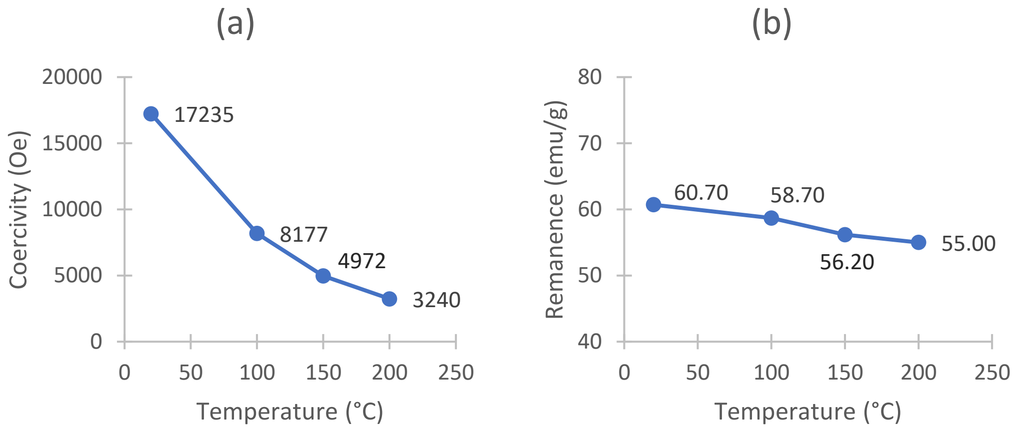

Figure 35: : Coercivity (a) and remanence (b) values of $Nd_{13.6}Fe_{73.6}Co_{6.6}B_{5.6}Ga_{0.6}$ *from 20°C up to 200°C with grain boundary diffusion* $Nd_{70}Cu_{30}$

We can observe that the coercivity increased from 12252 Oe up to 17235 Oe (40%) and the remanence decreased slightly from 71 emu/g to 60.7 emu/g (-15%). These results are interesting considering the fact that the coercivity temperature coefficient improved to -0.451%/°C. It was -0.490%/°C for the SPS process and it is even better than that of the melt-spun ribbons which was -0.471%/°C.

As previously discussed, the enhancement of coercivity is mainly attributed to the exchange decoupling of the $Nd_2Fe_{14}B$ grains as a result of the formation of the Nd-rich intergranular phase by the infiltration of eutectic melt. Moreover, since the temperature for grain boundary diffusion is lower than the one used for SPS or HD, the grain growth is inhibited. This would explain the better thermal stability obtained after grain boundary diffusion.

4.5.2. Grain boundary diffusion process applied to $Nd_{13.6}Fe_{73.6}Co_{6.6}B_{5.6}Ga_{0.6}$ with $Pr_{68}Cu_{25}Al_7$

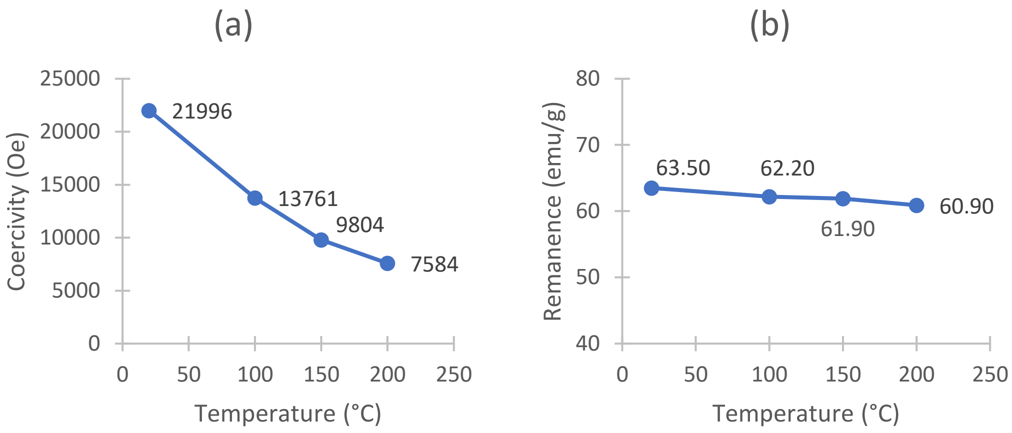

Figure 36: Coercivity (a) and remanence (b) values of $Nd_{13.6}Fe_{73.6}Co_{6.6}B_{5.6}Ga_{0.6}$ from 20°C up to 200°C with grain boundary diffusion $Pr_{68}Cu_{25}Al_7$

The diffusion of Pr-Cu-Al decreases the magnetic exchange interaction between the hard magnetic grains and therefore improves the coercivity. According to Fick's Law, Pr diffuses faster than Al and Cu along the grain boundary.

The results for this sample with Pr-Cu-Al diffusion are better than those obtained with the two-alloy method (4.3.3).

Grain boundary diffusion provided an enhancement in coercivity by about 20% with a reduction of less than 5% in remanence compared to the two-alloy method.

The temperature coefficient was -0.364%/°C for this sample. It was -0.519%/°C after the SPS process and -0.471%/°C for the melt-spun ribbons.

4.5.3. Grain boundary diffusion process applied with $Nd_{62}Dy_{20}Al_{18}$ to $Nd_8Fe_{87}Nb_{0.5}Zr_{0.5}B_4$ with 5wt.% $Nd_{70}Cu_{30}$ after SPS and hot deformation processes

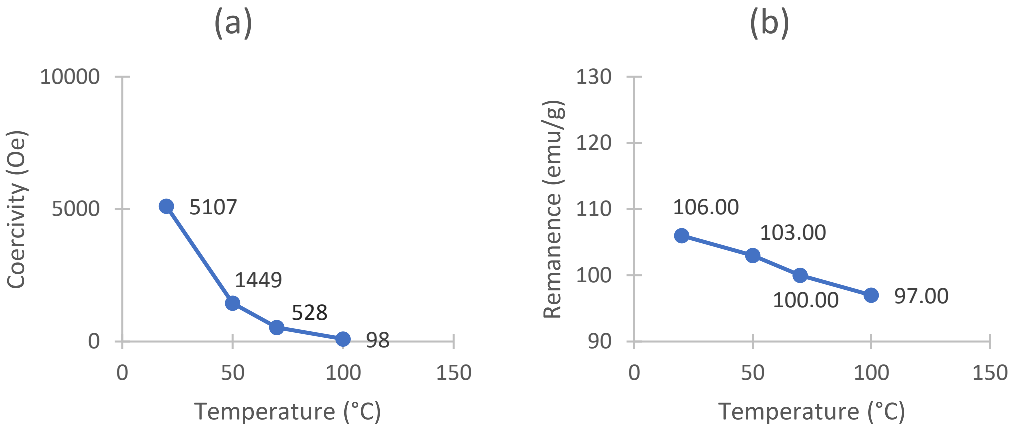

Figure 37: Coercivity (a) and remanence (b) values of $Nd_8Fe_{87}Nb_{0.5}Zr_{0.5}B_4$ with 5wt.% $Nd_{70}Cu_{30}$ from 20°C up to 100°C after HD and GBD

The improvement of coercivity was attributed to the Nd and Dy in the diffusion source. The behavior was the same as the other cases of grain boundary diffusion: Nd was diffused along the grain boundaries between $Nd_2Fe_{14}B$ grains and led to decoupling, therefore, increasing the coercivity (more than 50%). The Dy was also diffused along the grain boundaries and partially substituted Nd with Dy in the $Nd_2Fe_{14}B$ grains to form a shell that has a higher anisotropy field than $Nd_2Fe_{14}B$. On the other hand, decoupling led to a small decrease of remanence (less than 10%). Another reason remanence decreased is the antiferromagnetic coupling of Dy in the intergranular phase and Fe in $Nd_2Fe_{14}B$ grains.

Even if the results were already not good for the thermal stability after SPS+HD combined, we can observe that the grain boundary diffusion had no major impact on the coercivity temperature coefficient. It went from -1.235%/°C (after HD) to -1.226%/°C.

4.5.4. Grain boundary diffusion process applied with $Nd_{62}Dy_{20}Al_{18}$ to $Nd_7Dy_1Fe_{87}Nb_{0.5}Zr_{0.5}B_4$ with 5wt.% $Nd_{70}Cu_{30}$ after SPS and hot deformation processes

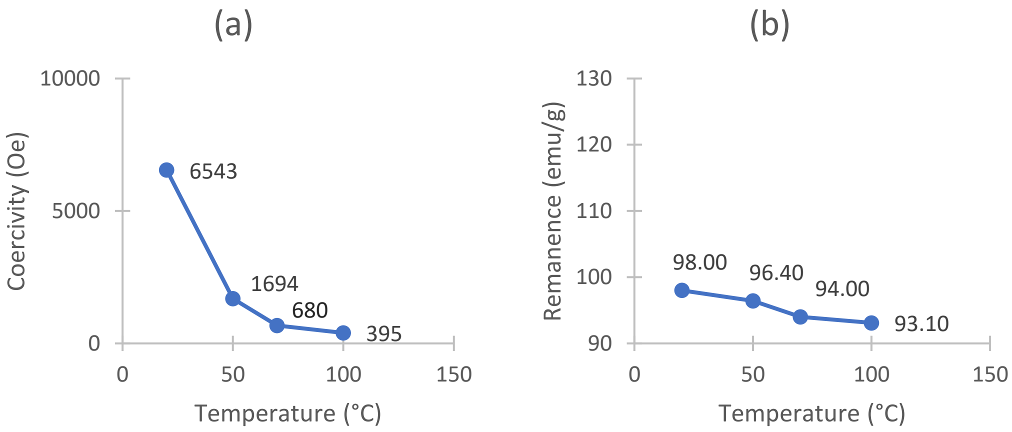

Figure 38: Coercivity (a) and remanence (b) values of $Nd_7Dy_1Fe_{87}Nb_{0.5}Zr_{0.5}B_4$ with 5wt.% $Nd_{70}Cu_{30}$ from 20°C up to 100°C after HD and GBD

Since the introduction of Dy had already increased the coercivity to a higher value when compared with that of the original sample, it was further improved by grain boundary diffusion. In the same way, the grain boundary diffusion improved the thermal stability. The coercivity temperature coefficient was improved from -1.226%/°C after HD to -1.175%/°C. It was -1.183%/°C after SPS.

4.5.5. Discussion

The grain boundary diffusion process showed good results for all SPS processed samples and hot deformed samples. In all cases, the low-melting-point alloy diffused in the grain boundaries, led to decoupling, and therefore, increased the coercivity of the samples at room temperature.

Concerning the SPS processed samples, the coercivity temperature coefficient improved. It showed better results than the two alloys method due mostly to the lower temperature during the process.

When the grain boundary diffusion was applied to hot deformed samples, the coercivity still improved but the process did not influence the coercivity temperature coefficient.

4.6. Comparative data on coercivity temperature coefficients and discussion

All the coercivity temperature coefficients and the processes that were used on the main samples are listed in Table 7.

This table is made to be read from top to bottom, starting with the basic composition of each sample, followed by the processes applied one after another to the sample. When the cell is grey, the process was not applied to the sample.

Concerning the sample $Nd_7Dy_1Fe_{87}Nb_{0.5}Zr_{0.5}B_4$, there is no data concerning the melt-spun sample and it was not produced again in order to avoid wasting rare-earth element.

When it is mentioned N/A, no results were obtained due to the coercivity reaching a zero value.

Table 8: Comparative data on coercivity temperature coefficients

	Sample composition		$Nd_8Fe_{87}Nb_{0.5}Zr_{0.5}B_4$		$Nd_7Dy_1Fe_{87}Nb_{0.5}Zr_{0.5}B_4$	$Nd_{13.6}Fe_{73.6}Co_{6.6}B_{5.6}Ga_{0.6}$				$Nd_{13}Dy_2Fe_{72.2}Co_{6.6}B_{5.6}Ga_{0.6}$
Applied processes	**Melt spinning and annealing**	Coercivity temperature coefficient (20-100°C)	-1.032%/°C		---	-0.583%/°C				-0.391%/°C
		Coercivity temperature coefficient (20-200°C)	N/A		---	-0.471%/°C				-0.388%/°C
	Spark plasma sintering process (SPS)	With or without low-melting-point alloy	No low-melting-point alloy addition	5wt.% $Nd_{70}Cu_{30}$	5wt.% $Nd_{70}Cu_{30}$	No low-melting-point alloy addition			10w.% $Pr_{68}Cu_{25}Al_7$	
		Coercivity temperature coefficient (20-100°C)	N/A	-1.224%/°C	-1.183%/°C	-0.667			-0.68%/°C	
		Coercivity temperature coefficient (20-200°C)	N/A	N/A	N/A	-0.490			-0.519%/°C	
	Hot deformation process (HD)	Coercivity temperature coefficient (20-100°C)		-1.235%/°C	-1.226%/°C	-0.735 %/°C			-0.563%/°C	
		Coercivity temperature coefficient (20-200°C)		N/A	N/A	-0.522 %/°C			-0.526%/°C	
	Grain boundary diffusion process (GBD)	Alloy diffusion		$Nd_{62}Dy_{20}Al_{18}$	$Nd_{62}Dy_{20}Al_{18}$		$Nd_{70}Cu_{30}$	$Pr_{68}Cu_{25}Al_7$		
		Coercivity temperature coefficient (20-100°C)		-1.226%/°C	-1.175%/°C		-0.657%/°C	-0.468%/°C		
		Coercivity temperature coefficient (20-200°C)		N/A	N/A		-0.451%/°C	-0.364%/°C		

To begin with, we will discuss the processes that were applied to the samples during this study.

First, during the SPS process, the localized high heating led to an uneven grain growth and a loss of uniformity in the microstructure. This led to a decrease of coercivity as well as a loss of thermal stability for all samples. To reduce the grain growth, low melting point alloys such as $Nd_{70}Cu_{30}$ and $Pr_{68}Cu_{25}Al_7$ were used during SPS process. In the case of $Nd_{70}Cu_{30}$, it improved the thermal stability and the coercivity of the sample because the low-melting-point alloy diffused along the grain boundary phase during the SPS process and assisted in maintaining the uniform microstructure as well as isolating the $Nd_2Fe_{14}B$ grains. However, in the case of $Pr_{68}Cu_{25}Al_7$, it improved the coercivity of the sample but decreased the thermal stability of the sample, partly due to the dissolution of Al in the $Nd_2Fe_{14}B$ phase. Therefore, we can conclude that using $Nd_{70}Cu_{30}$ as a low melting point alloy has good results but the SPS-processed samples with low-melting point alloy still presented worse results than the melt-spun ribbons of the same compositions.

Second, the hot deformation process was applied on SPS-processed samples. Previous studies have shown that the hot deformation process reduces the coercivity of the samples due to grain growth. In this study, the goal was to study the impact that hot deformation had on the thermal stability of the samples. It showed that hot deformation did not improve at all the thermal stability of the samples, on the contrary. All hot-deformed samples presented a decrease of thermal stability. Therefore, this process is not viable to for elevated temperature application permanent magnets, and the combination of SPS process and HD process is not suitable to obtain a better thermal stability. In some recent study, Zheng et al. [55] discovered that coercivity of hot deformed Nd-Fe-B samples can be increased by using alloys with a high melting point as hot-pressed precursors to inhibit the growth of coarse grains. They obtained a coercivity around 12 kOe at room temperature after hot deformation. At the optimal hot pressing temperature (550°C), the hot-deformed magnet gained the optimum alignment and the stacked platelet-shaped grains were separated by smooth thin grain boundary. They did not study the thermal stability of the samples but this microstructure of the magnet might lead to a better thermal stability. Indeed, grain refinement and the optimization of grain boundaries can eliminate ferromagnetic phases and surface defects, and are among the most effective procedures for increasing the coercivity. Therefore, this could be an interesting process to observe, more especially its impact on the thermal stability.

Third, the grain boundary diffusion process was applied to some SPS-processed and hot-deformed samples. For all samples, we observed an improvement of the thermal stability. For the hot-deformed samples, the thermal stability was still improved but as previously discussed, applying hot deformation after SPS is not a suitable process. For these samples, $Nd_{62}Dy_{20}Al_{18}$ was used. Even if we applied it only to SPS-processed samples, due to the higher content of Al and the diffusion of Al into the $Nd_2Fe_{14}B$ main phase, the thermal stability of coercivity could be inferior to that using $Nd_{70}Cu_{30}$ alloy or $Pr_{68}Cu_{25}Al_7$. It would be interesting to verify that theory but once again, using rare-earth element is a current issue in this domain and it would be preferable to study alternative solutions.

For the SPS-processed samples, using $Nd_{70}Cu_{30}$ and $Pr_{68}Cu_{25}Al_7$ showed great improvement of thermal stability. It was even better than the coercivity of the melt-spun ribbons. As previously discussed, with $Nd_{70}Cu_{30}$, the enhancement of coercivity is mainly attributed to the exchange decoupling of $Nd_2Fe_{14}B$ grains as a result of the formation of the Nd-rich intergranular phase by the infiltration of eutectic melt. To apply grain boundary diffusion, the temperature of the process is lower than SPS or HD, and therefore, inhibits grain growth. With $Pr_{68}Cu_{25}Al_7$, regions of coarse grains were reduced and overall grain refinement was observed after the addition of $Pr_{68}Cu_{25}Al_7$ [37], leading to an enhancement of coercivity and thermal stability. The best results of thermal stability were realized with the addition of $Pr_{68}Cu_{25}Al_7$ on the sample $Nd_{13.6}Fe_{73.6}Co_{6.6}B_{5.6}Ga_{0.6}$ after SPS processing. However, it is possible to apply grain boundary diffusion directly on melt-spun ribbons and avoid the negative impact of SPS processing. Xie et al. [56] studied the coercivity enhancement and the thermal stability improvement in the melt-spun $Nd_{12}Fe_{77.5}Co_5B_{5.5}$ ribbons with $Nd_{70}Cu_{30}$ grain boundary diffusion and obtained a coercivity temperature coefficient of -0.32%/°C (200-150°C). Since SPS processing decrease the thermal stability of the sample, using directly grain boundary diffusion on the melt-spun ribbons seems to be a suitable process. It would be interesting to try the grain boundary diffusion of $Nd_{13.6}Fe_{73.6}Co_{6.6}B_{5.6}Ga_{0.6}$ with $Nd_{70}Cu_{30}$ without SPS process and to compare those results with the literature. Moreover, since we obtained great results with $Pr_{68}Cu_{25}Al_7$, it would be also interesting to apply grain boundary diffusion to $Nd_{13.6}Fe_{73.6}Co_{6.6}B_{5.6}Ga_{0.6}$ in order to compare it. Another option would be to use the grain boundary diffusion of heavy rare-earth, such as Dy or Tb, but it is still the same discussion with the use of rare-earth elements. It is an issue in the production of permanent magnets, not only for the quantity of rare-earth elements available but also for the raise of the costs of the magnet. Wan et al. [57] obtained good results with $Pr_{65}Cu_{35}$ and there would be no risk of Al dissolution in that case, therefore, it could be interesting to try this grain boundary diffusion on $Nd_{13.6}Fe_{73.6}Co_{6.6}B_{5.6}Ga_{0.6}$ to compare the results and observe the effect of Al in the grain boundary diffusion, related to its amount.

For this study, processes had an impact on the results but also the chemical composition of the samples. It seems that a higher Nd content played a role in separating the $Nd_2Fe_{14}B$ grains with the Nd-rich intergranular phase, leading to a better coercivity. The Nd content should be above 12 at.%. Moreover, adding Dy to the composition led to good thermal stability results right after annealing. As previously discussed, melt-spun ribbons are sensitive to the addition of rare-earth elements and it had good results improving the thermal stability of the sample and its coercivity. It would be interesting to apply grain boundary diffusion with $Pr_{68}Cu_{25}Al_7$ to the $Nd_{13}Dy_2Fe_{72.2}Co_{6.6}B_{5.6}Ga_{0.6}$ because the coercivity temperature coefficient of the melt-spun ribbons was the best we obtained in this study: -0.388%/°C (20-200°C). However, once again, using rare-earth element could raise the cost of the magnet and this is an issue at stake.

5. Conclusions

In this research, different compositions of Nd-Fe-B magnets with $Nd_2Fe_{14}B$ hard magnetic phase and soft magnetic α-Fe phase were produced and analyzed. The composition $Nd_{13.6}Fe_{73.6}Co_{6.6}B_{5.6}Ga_{0.6}$ provided the good results in this study with a temperature coefficient of coercivity of -0.47%/°C for the melt-spun sample and without earth-rare elements.

The combination of Dy, Co, and Ga with a 0.2 atomic percentage of Dy ($Nd_{13}Dy_2Fe_{72.2}Co_{6.6}B_{5.6}Ga_{0.6}$) resulted in a temperature coefficient of coercivity of -0.39 %/°C. With an annealing at 610°C, this seems to be the best composition to start with for a better thermal stability. Applying the following successful processes on $Nd_{13}Dy_2Fe_{72.2}Co_{6.6}B_{5.6}Ga_{0.6}$ could possibly improve the results we obtained at the end.

When it is concerning the thermal stability, SPS seems to deteriorate the temperature coefficients. Applying this process without $Nd_{70}Cu_{30}$ low-melting-point alloy gives poor results. In order to improve the process, it could be interesting to try using Dy-Cu alloy instead of Nd-Cu since it had good results in previous studies and Dy is a central element when the thermal stability is at stake.

However, nowadays, the use of Nd-Fe-B magnets without rare-earth element is also a problem in terms of thermal stability.

Hot deformation did not provide any improvement at all. It is not suitable for high-temperature applications.

Grain boundary diffusion was, on the contrary very successful. The decoupling of the $Nd_2Fe_{14}B$ grains and the diffusion along the intergranular region led to an increase of coercivity. The problem in grain boundary diffusion is that the reduction of remanence will also occur because of the decrease of the volume fraction of the ferromagnetic phase. Minimizing the reduction of remanence while obtaining high coercivity may be a challenge for future research. However, the results remained positive and the best one was obtained using $Pr_{68}Cu_{25}Al_7$ on $Nd_{13.6}Fe_{73.6}Co_{6.6}B_{5.6}Ga_{0.6}$ with a temperature coefficient of coercivity of -0.36 %/°C.

6. References

[1] Matthis, D. C., The theory of magnetism I, vol. 17, Springer Series in Solid-State Science, 1981, pp. 1-38.

[2] Smith, Peter J., "The beginning of experimental studies of magnetism in Europe," *Earth-Science Reviews,* vol. 6, pp. A11-A18, February 1970.

[3] Coey, J. M. C., "Magnetism in future," *Journal of Magnetism and Magnetic Materials,* pp. 226-230, 2001.

[4] Cullity, B.D.; Graham, C. D., Introduction to Magnetic Materials, Second ed., IEEE Press, 2009, pp. 1-23.

[5] Mukherjee, Santanu, "Analysis of mechanically milled exchange coupled nanocomposite permanent magnets," University of Lincoln, Nebraska, 2011.

[6] Jiles, D., Introduction to magnetism and magnetic materials, 3 ed., C. Press, Ed., 2016, pp. 83-100.

[7] Spaldin, N., Magnetic materials: fundamental and device applications, C. u. press, Ed., 2003, pp. 1-15.

[8] Bornhoft, J. M., "Nd-Fe-B Nanoparticles through Surfactant Assisted Mechanical Milling and Alloy Design," University of Lincoln, Nebraska, 2013.

[9] Rudowicz, H. W. F. Sung C., "Physics behind the magnetic hysteresis loop: a survey of misconceptions in magnetism literature," *Journal of magnetism and magnetic materials,* no. 260, pp. 250-260, 2003.

[10] Skomski, R., Simple Models of Magnetism, Oxfort University Press, 2008, pp. 73-100.

[11] Coey, J. M. D., Magnetism and magnetic materials, C. u. press, Ed., 2009, pp. 168-195.

[12] Golkar-Fard, F. R., "Mechanical milling of co-rich melt-spun Sm-Co alloys," University of Lincoln, Nebraska, 2010.

[13] Anderon, J. J., "Structural and magnetic properties of neodymium - iron - boron clusters," University of Lincoln, Nebraska, 2010.

[14] T., Mishima, "Nickel-aluminum steel for permanent magnets," *Stahl Eisen,* vol. 53, p. 79, 1931.

[15] Ravindran V.K., Shield J.E., "Rapid Soldificaton of Sm-Co permanent magnets. Lincoln :," *Phase Transformations in Magnetic Materials,* vol. Metallurgical and materials transactions, pp. 732-737, 2007.

[16] Strnat K., Hoffer G., Olson J., et al., "A family of new cobalt-base permanent," *Journal of Applied Physic,* vol. 38, p. 1001, 1967.

[17] H. A. Leupold, E. Potenziani, and A. TauberH. F. Mildrum, "High coercivity 2-17 cobalt rare-earth magnets," *Journal of Applied Physics,* vol. 55, p. 2097, 1984.

[18] R. Madugundo, N. Venkata, R. Rao, A.M. Schönhöbel, D. Salazar, A. A.El-Gendy, "Recent developments in nanostructured permanent magnet Materials and Their Processing Methods," in *Magnetic Nanostructured Materials*, 2018, pp. 157-198.

[19] R. W. Gao,W. C. Feng, H. Q. Liu, B. Wang, W. Chen, G. B. Han,P. Zhang, H. Li, "Exchange-coupling interaction, effective anisotropy and coercivity in nanocomposites permanent materials," *Journal of Applied Physics,* vol. 94, p. 664, 2003.

[20] S. Mukherjee, Analysis of mechanically milled exchange coupled nanocomposites permanent magnets, University of Nebraska Lincoln, 2012.

[21] Kneller, E.F. and R. Hawig, R., "The exchange spring magnet: a new material principle for permanent magnets," *IEEE Transactions,* vol. 27, pp. 3588-3560, 1991.

[22] S. Pandian, V. Chandrasekaran, G. Markandeyulu, K.J.L. Iyer, K.V.S. Rama Rao, "Effect of Co, Dy and Ga on the magnetic properties and the microstructure of powder metallurgically processed Nd-Fe-B magnets," *Journal of Alloys and Compounds,* vol. 364, pp. 295-303, 2004.

[23] G. Bai, R.W. Gao, Y. Sun, G.B. Han, B. Wang, "Study of high-coercivity sintered NdFeB magnets," *Journal of Magnetism and Magnetic Materials,* vol. 308, p. 20–23, 2007.

[24] S.Z. Zhou, Q.F. Dong,, Supermagnets: Rare-earth and Iron System Permanent Magnet, p. 272, 1999, p. 272.

[25] S. Sugimoto, "Current status and recent topics of rare-earth permanent magnets," *Journal of Physics D: Applied physics,* vol. 44, pp. 064001-064011, 2011.

[26] D N Brown, Z Wu, F He, D J Miller, J W Herchenroeder, "Dysprosium-free melt-spun permanent magnets," *Journal of Physics: Condensed Matter,* vol. 26, p. 064202, 2014.

[27] R.S. Mottram, A. Kianvash, I.R. Harris, "The use of metal hydrides in powder blending for the production of Nd-Fe-B magnets," *Journal of Alloys and Compounds ,* vol. 283, p. 282–288, 1999.

[28] A.K. Mukherjee, A.V. Sergueeva, D.M. Hulbert, N.A. Mara, "Mechanical properties of nanocomposite materials," *Frontiers of Nanosciences,* vol. 1, pp. 127-172, 2009.

[29] A. V. Ragulya, "Fundamentals of Spark Plasma Sintering," in *Encyclopedia of Materials: Science and Technology*, 2010, pp. 1-5.

[30] Tokita M., "Spark Plasma Sintering (SPS) Method, Systems, and Applications," in *Handbook of Advanced Ceramics*, 2013, pp. 1149-1177.

[31] Z. A. Munir, U. Anselmi-Tamburini, M. Ohyanagi, "The Effect of Electric Field and Pressure on the Synthesis and Consolidation of Materials: A Review of the Spark Plasma Sintering Method," *Journal of Materials Science ,* vol. 41, pp. 763-777, 2006.

[32] M. Yue, J.X. Zhang, W.Q. Liu,, G.P. Wang, "Chemical stability and microstructure of Nd-Fe-B magnet prepared by spark plasma sintering," *Journal of Magnetism and Magnetic Materials,* vol. 271, pp. 364-368, 2004.

[33] Z W Liu, H Y Huang, X X Gao,H Y Yu, X C Zhong, J Zhu, D C Zeng, "Microstructure and property evolution of isotropic and anisotropic NdFeB magnets fabricated from nanocrystalline ribbons by spark plasma sintering and hot deformation," *Journal of Physics D Applied Physics,* vol. 44, p. 025003, 2011.

[34] T. Akiya, J. Liu, H. Sepehri-Amin, et al, "Low temp diffusion processs using rare earth-Cu eutectic alloys for hot-deformed Nd-Fe-B bulk magnets," *Journal of Applied Physics,* vol. 115, p. 17A766, 2014.

[35] Y. I. Lee, H. W. Chang, G. Y. Huang, C. W. Shih, W. C. Chang, "Comparison on the Coercivity Enhancement of Hot-Deformed Nd2Fe14B-Type Magnets by Doping R70Cu30 (R = Nd, Dy, and Tb) Alloy Powders," *IEEE Transactions on magnetic,* vol. 53, no. 11, 2017.

[36] H. S.-A. T. O. e. a. L. Liu, "Coercivity enhancement of hot-deformed Nd-Fe-B magnet by the eutectic grain boundary diffusion process using Nd 62 Dy 20 Al 18 alloy," *Scripta Materialia,* vol. 129, pp. 44-47, 2017.

[37] L. Zhang, M. Wang, X. Yan, Y. Lin, J. Shield, "Effect of low-melting point phases on the microstructure and properties of spark plasma sintered and hot deformed Nd-Fe-B alloys," *Journal of Magnetism and Magnetic Materials,* 2017.

[38] R.W. Lee, "Hot-pressed neodymium-iron-boron magnets," *Applied Physics Letters,* 1985.

[39] K Hioki, A Hattori, T Iriyama, "Development of Dy-Free Hot-Deformed Nd-Fe-B Magnets by Optimizing Chemical Composition and Microstructure," *Journal of the magnetics ,* vol. 3, no. 1, p. 38, 2014.

[40] X-Q Li, L. Li, K. Hu, Z-C Chen, S-G uU, C. Yang, "Microstructure and magnetic properties of anisotropic Nd−Fe−B magnets prepared by spark plasma sintering and hot deformation," *Transactions of Nonferrous Metals Society of China,* vol. 24, pp. 3142-3151, 2014.

[41] W. Q. Liu, Z. Z. Cui, X. F. Yi, M. Yue, Y. B. Jiang, D. T. Zhang, J. X. Zhang, and X. B. Liu, "Structure and magnetic properties of magnetically isotropic and anisotropic Nd–Fe–B permanent magnets prepared by spark plasma sintering technology," *Journal of Applied Physics ,* vol. 107, p. 09A719, 2010.

[42] Y.H. Hou, Y.L. Huang, Z.W. Liu, D.C. Zeng, S.C. Ma, Z.C. Zhong, "Hot deformed anisotropic nanocrystalline NdFeB based magnets prepared from spark plasma sintered melt spun powders," *Materials Science and Engineering B,* vol. 178, pp. 990-997, 2013.

[43] Y. L. Huang, Z. W. Liu, X. C. Zhong, et al. , "Diffusion of Nd-rich phase in the spark plasma sintered and hot deformed nanocrystalline NdFeB magnets.," *Journal of Applied Physics,* vol. 111, p. 033913, 2012.

[44] L. Liu, H. Sepehri-Amin, T. T. Sasaki, T. Ohkubo, M. Yano, N. Sakuma, A. Kato, T. Shoji, and K. Hono, "Coercivity enhancement of Nd-Fe-B hot-deformed magnets by the eutectic grain boundary diffusion process using Nd-Ga-Cu and Nd-Fe-Ga-Cu alloys," *AIP Advances ,* vol. 8, p. 056205, 2018.

[45] U.M.R.Seelam, L. Liu, T.Akiya, H.Sepehri-Amin, T.Ohkubo, N.Sakuma, M.Yano, A.Kato, K.Hono, "Coercivity of the Nd–Fe–B hot-deformed magnets diffusion-processed with low melting temperature glass forming alloys," *Journal of Magnetism and Magnetic Materials,* vol. 412, pp. 234-242, 2016.

[46] H. Nakamura ; K. Hirota ; M. Shimao ; T. Minowa ; M. Honshima, "Magnetic properties of extremely small Nd-Fe-B sintered magnets," *IEEE Transactions on Magnetics,* vol. 41, pp. 3844 - 3846, 2005.

[47] J.Lia, L. Liu, H. Sepehri-Amina, X. Tang, T.Ohkubo, N.Sakuma, T.Shoji, A.Kato, T.Schrefl, K.Hono, "Coercivity and its thermal stability of NdFeB hot-deformed magnets enhanced by the eutectic grain boundary diffusion process," *Acta Materialia,* vol. 161, pp. 171-181, 2018.

[48] H. Sepehri-Amin, T. Ohkubo, S. Nagashima et al., "High-coercivity ultrafine-grained anisotropic Nd-Fe-B magnets processed by hot deformation and the Nd-Cu grain boundary diffusion process.," *Acta Materialia,* vol. 61, pp. 6622-6634, 2013.

[49] H.Sepehri-Amin, J.Liu, T.Ohkubo, K.Hioki, A.Hattori, K.Hono, "Enhancement of coercivity of hot-deformed Nd–Fe–B anisotropic magnet by low-temperature grain boundary diffusion of Nd60Dy20Cu20 eutectic alloy," *Scripta Materialia,* vol. 69, pp. 647-650, 2013.

[50] Y. Geng, Microstructure and magnetic behavior studies of processing-controlled and composition-modified Fe-Ni and Mn-Al alloys, University of Nebraska Lincoln, 2014.

[51] Y. Lin, "Magnetic Properties of Hot Deformed and Boundary Diffused Nd-Fe-B Permanent Magnet," *University of Nebraska-Lincoln,* 2017.

[52] S. Ur Rehman; Q. Jiang; W. Lei; L. Zeng; Q. Tan; M. Ghazanfar, S.U. Awan; T. Ahmad, M. Zhong; Z. Zhong, "Microstructure, magnetic properties, thermal stabilities and coercivity mechanisms of Ta doped Nd-Fe-B ribbons," *Journal of Physics and Chemistry of Solids,* January 2019.

[53] X.Song, X. Liu, and J.Zhang, "Neck formation and self adjusting mechanism of neck growth of conducting powders in spark plasma sintering," *J. Am. Ceram. Soc.,* vol. 89, no. 2, pp. 494-500, 2006.

[54] J. Liu, H. Spehri-Amin, T. Ohkubo, K. Hioki, A. Hattori, T. Schrefl and K. Hono, "Grain size dependence of coercivity of hot deformed Nd-Fe-B anisotropic magnets," *Acta Matter,* vol. 82, pp. 336-343, 2015.

[55] Zheng X F, Li M, Chen R J, Lei F, Jin C X, Wang Z X, Ju J Y, Yin W Z, Lee D and Yan A R 2017, "Effects of hot pressing temperature on the alignment and phase composition of hot-deformed nanocrystalline Nd-Fe-B magnets," *Journal of Magnetism and Magnetic Materials,* vol. 488, 2019.

[56] J. Xie, C. Yuan, Y. Luo, Y. Yang, B. Hu, D. Yu, W. Yan, "Coercivity enhancement and thermal-stability improvement in the melt-spun NdFeB ribbons by grain boundary diffusion," *Journal of magnetism and magnetic materials,* vol. 446, pp. 210-213, 2018.

[57] F. Wan, Y.Zhang, J. Han, et al. , "Coercivity enhancement in Dy-free Nd-Fe-B sintered magnets by using Pr-Cu alloys," *Journal of applied physics,* p. 111, 2012.

[58] Walmar, Marlin S., Chen, Christina H. and Walmar, Michael H., "A new class of Sm-TM magnets for operating temperatures up to 550C," *IEEE Transactions on magnetics, ,* vol. 36, 2000.

[59] Y. Matsuura, "Recent development of Nd–Fe–B sintered magnets and their applications," *Journal of Magnetism: Magnetic Materials,* vol. 303, pp. 344-347, 2006.